

LIBRARY
ROYAL AIRCRAFT ESTABLISHMENT
BEDFORD.



MINISTRY OF AVIATION

AERONAUTICAL RESEARCH COUNCIL

CURRENT PAPERS

AERODYNAMIC STUDY

Force and Moment
Measurements on Three Delta Wings
of Aspect Ratios 0.83, 1.03 and 1.24 in
Combination with Bodies of Fineness Ratio
13 at a Mach Number of 4

by

D. R. Andrews

LONDON: HER MAJESTY'S STATIONERY OFFICE

1966

SEVEN SHILLINGS NET

AERODYNAMIC STUDY - FORCE AND MOMENT MEASUREMENTS ON THREE DELTA WINGS
OF ASPECT RATIOS 0.83, 1.03 AND 1.24 IN COMBINATION WITH BODIES OF
FINENESS RATIO 13 AT A MACH NUMBER OF 4.

by

D.R. Andrews

SUMMARY

Force measurements have been made in the High Supersonic Speed Wind Tunnel on a series of wing-body configurations at a Mach number of 4 and Reynolds number of 32×10^6 . The combinations tested consisted of circular section bodies of fineness ratio 13 and delta wings of aspect ratios 0.83, 1.03 and 1.24. The wing span of all combinations was 5 body diameters.

Lift and pitching moment variations with incidence were found to be reasonably linear up to 20° , which was the limit of the present tests. The highest lift/drag ratio was obtained with the lowest aspect ratio wing, giving a figure of 5.7 for a 3 calibre ogival nose on the body and 6.2 for a 5 calibre nose. It was found that the force and moment characteristics could in general be predicted adequately from existing theories, the main exception being the rolling moment due to sideslip.

<u>LIST OF CONTENTS</u>		<u>Page</u>
1	INTRODUCTION	4
2	DESCRIPTION OF MODELS TESTED	4
3	EXPERIMENTAL DETAILS	5
	3.1 Scope of tests	5
	3.2 Corrections to and accuracy of results	5
4	RESULTS AND DISCUSSION	6
	4.1 Body alone	6
	4.2 Wing and body	8
	4.2.1 Longitudinal and drag characteristics	8
	4.2.2 Lateral and directional characteristics	9
	4.2.3 Flow field around models	11
5	FURTHER WORK	12
6	CONCLUSIONS	12
	LIST OF SYMBOLS	13
	LIST OF REFERENCES	14

TABLE 1 - Details of bodies and wings tested 16

ILLUSTRATIONS - Figs. 1-18

DETACHABLE ABSTRACT CARDS

<u>LIST OF ILLUSTRATIONS</u>		<u>Fig.</u>
Force and moment reference axes		1
Model configurations tested		2
Configuration B _{1b} W ₁ mounted in the tunnel		3
Normal force coefficient for body alone		4
Pitching moment coefficient for body alone		5
Normal force coefficient versus incidence for wing-body configurations at zero sideslip		6
Pitching moment coefficient versus incidence for wing-body configurations at zero sideslip		7
Centre of pressure position measured from body vertex		8
Effect of Reynolds number on zero-lift drag		
(a) body with 3D nose		
(b) body with 5D nose		9
Axial force variation with incidence		10

<u>LIST OF ILLUSTRATIONS (Contd)</u>	<u>Fig.</u>
Effect of sideslip angle on axial force at zero lift	11
Lift to drag ratios	12
Side force coefficient	13
Yawing moment coefficient referred to body axes	14
Centre of pressure of side force	15
Rolling moment coefficient referred to body axes	16
Schlieren photos showing side view of model with 3 calibre nose and aspect ratio 1.03 wing (B_{1a} W_2) at zero sideslip	17
Location of body vortices and wing and body shocks (a) at body base (b) at 3 body dias. upstream of body base	18

1 INTRODUCTION

A programme of wind tunnel research is being undertaken on a common series of models in the 8 ft x 8 ft and High Supersonic Speed Tunnels at Bedford. Tests at Mach numbers up to 2.8 are provided by the 8 ft tunnel and at Mach 4 by the H.S.S.T. with its present fixed nozzle.

The programme of tests is aimed at the investigation of slender wing-body configurations.

For the first series of models to be built, the body length and diameter and the wing span have been kept constant, and the wing sweep-back and the fineness ratio of the body nose varied. Measurements of the overall forces and moments on these models were made at a Mach number of 4 in the 4 ft x 3 ft High Supersonic Speed Wind Tunnel, incidences up to 20° and sideslip angles up to 10° being covered. The results of these tests are presented in this Note and a comparison made with theoretical predictions wherever possible.

2 DESCRIPTION OF MODELS TESTED

Fig.2 shows the various model configurations tested and Table 1 lists the relevant dimensions.

The basic configuration of wing W_1 on body B_{1a} , which forms a convenient starting point to the series, is approximately a $\frac{1}{4}$ scale model of a possible design of long-range missile. It consists of a body of circular cross section with an ogival* nose of length $3d$, the overall body length being $13d$. The value of d , the body diameter, is 3.70 in. model scale. The wing span is $5d$ and the leading edge sweepback angle, ϕ , such that

$M^2 - 1. \cot\phi$ is 0.8 at $M = 4$. The wing thickness is constant with the leading and trailing edges chamfered at an included angle of 15°.

Wings W_2 and W_3 were also tested on body B_{1a} , these wings having the same span as W_1 but smaller root chords such that $M^2 - 1. \cot\phi$ has the values 1.0 for W_2 and 1.2 for W_3 .

A $5d$ ogival* nose (body B_{1b}) was tested with wing W_1 , the overall body length remaining the same at $13d$.

Finally, the body alone was tested with each of the ogival noses.

It should be noted that the dimensions given in Fig.2 are nominal values assuming zero leading and trailing edge thickness. To obviate

* Although referred to as ogival throughout this note, the nose shapes are in fact cubic and of the equations given in Table 1. The difference between the cubic and tangent ogive shapes is small.

damage to the model, a small radius was put on the edges: this results in the measured dimensions given in Table 1 being slightly less than the nominal values.

Fig. 3 shows configuration B_{1b} W₁ mounted from the quadrant of the tunnel.

3 EXPERIMENTAL DETAILS

3.1 Scope of tests

The tests were made at $M = 3.97$ in the High Supersonic Speed Wind Tunnel at R.A.E. Bedford. Results were obtained up to a maximum incidence of between 20° and 25° , depending on the configuration, the maximum incidence that could be used being dictated by maximum balance load considerations or by the limit of travel of the quadrant (25°). Sideslip angles of 0 , $\pm 5^\circ$ and $\pm 10^\circ$ were covered. The tests were made at total pressures of 45 and 180 in. Hg absolute, corresponding to Reynolds numbers based on body length of 8.0×10^6 and 32.0×10^6 respectively. In addition zero-lift drag measurements were made over a range of total pressures corresponding to Reynolds numbers from 2×10^6 to 32×10^6 .

The total temperature was constant at 40°C and the frost point varied in the range -33°C to -45°C .

To fix transition, roughness was applied to the wings over a region extending from $1/16$ in. to $5/16$ in. from the leading edges and on the body from $1/4$ in. to $1/2$ in. from the nose. The roughness was produced by 60 grade carborundum particles (approx. 0.010 in. size) fixed to the surface with a thin layer of Araldite. As the variation of zero lift drag with Reynolds number was found to be consistent with wholly turbulent flow (Fig.9), it can be assumed that this roughness was sufficient to provoke transitions near the nose of the body and leading edge of the wings.

The overall forces on the model were measured with a 6 component strain gauge balance of $2\frac{1}{4}$ in. dia of the type described in Ref. 2. Base pressure was measured by measuring the pressure in the interior of the model. A brief pressure survey was made across the base of the model to ensure that this pressure gave a true mean value.

3.2 Corrections to and accuracy of results

The results have been corrected for sting deflection and balance interactions, and the axial force readings corrected to a base pressure equal to the free stream static pressure. The free stream static pressure was calculated from the Mach number and the measured total pressure, the Mach number being obtained by calibration of the working area of the tunnel using pitot tubes.

The reference area for force coefficients is the body cross sectional area, and the reference length for moments the diameter of the body. The reference centre for moments is at 7.604d from the body nose. Unless otherwise stated forces and moments are referred to the body axes system shown in Fig. 1.

The accuracy of the results obtained at a total pressure of 180 in. Hg ($R = 32 \times 10^6$) is estimated to be within the following limits:

	$\alpha = 0$	$\alpha = 20$
α		$\pm 0.1^\circ$
β		$\pm 0.1^\circ$
M		± 0.02
C_Z	± 0.1	± 0.3
C_X	± 0.02	± 0.02
C_Y	± 0.05	± 0.05
C_ℓ	± 0.1	± 0.1
C_m	± 0.1	± 0.5
C_n	± 0.1	± 0.1
\bar{x}/d	± 0.1 wing & body ± 0.5 body alone	± 0.05

The accuracy decreases when total pressure is reduced, and for axial force the following values have been estimated:

R/ft.	2×10^6	5×10^6	10×10^6	32×10^6
Possible errors in C_X	± 0.05	± 0.03	± 0.02	± 0.02

4. RESULTS AND DISCUSSION

The results obtained are shown in Figs. 4-16. As it was found that there was no significant Reynolds number effect on coefficients other than C_X , only the values for a Reynolds number of 32×10^6 have been presented in Figs. 4 to 8 and 10 to 16.

Owing to the fact that an incidence setting error of 0.3° was not allowed for in the computation, the results do not quite pass through the origin.

4.1 Body alone

The variation of $-C_Z$ and C_m with incidence for the body alone with the 3d and the 5d ogival noses is shown in Figs. 4 and 5, and the centre of pressure position shown in Fig. 8. The variations with incidence appear to be linear only over the first 4 or 5°. Above this angle, body vortices appear (as seen in the schlieren photos of Fig. 17): the normal force then increases more rapidly and the centre of pressure moves aft. At high incidence the centre of pressure approaches the centroid of the body plan area.

The table below compares the experimental values of $-\frac{dC_Z}{d\alpha}$, the slope of normal force coefficient, and \bar{x}/d , the centre of pressure position in body diameters from the nose, obtained at low incidence ($\alpha < 4^\circ$), with predictions from second order shock expansion theory³. This method has been found to give good agreement with experiment for

those combinations of body shape and Mach number which lie between the range of applicability of Van Dyke's second order potential theory and the generalised shock expansion theory. Also given are values from the empirical method of Ref. 4.

	3d nose			5d nose		
	Exp.	Theory Ref. 3	Theory Ref. 4	Exp.	Theory Ref. 3	Theory Ref. 4
$-\frac{dC_z}{d\alpha}$	3.6	3.4	3.4	3.2	3.2	3.2
\bar{x}/d	3.2	3.0	3.1	3.8	4.0	4.0

Agreement between the two estimated values and experiment is seen to be good, bearing in mind the accuracy of the experimental data.

Ref. 4 gives a semi-empirical method of estimating the normal force and pitching moment at high incidence, the variation of C_z and C_m being assumed to be of the form

$$(-C_z) = \left(-\frac{dC_z}{d\alpha} \right)_{\alpha=0} \sin\alpha \cos\alpha + F_1 F_2 \sin^2\alpha \quad (1)$$

$$C_m = \left(\frac{dC_m}{d\alpha} \right)_{\alpha=0} \sin\alpha \cos\alpha - G_1 G_2 \frac{\ell}{d} \sin^2\alpha \quad (2)$$

where F_1 and G_1 are based on Allen's cross-flow theory and F_2 and G_2 are empirical constants.

Figs. 4, 5 and 8 show that the agreement with experiment is reasonably good, any differences being within the limits of accuracy claimed for the method. However, the different shapes of the C_R/α curves (Fig. 8) suggests that the theory is not based on a true picture of the actual physical flow.

The variation of zero-lift drag with Reynolds number is shown in Figs. 9(a) and (b). For the two bodies B_{1a} and B_{1b} , excellent agreement is obtained with estimates made assuming turbulent flow from the body nose, the skin friction contribution being derived from Ref. 5 and the wave drag from Ref. 3. The wave drag contribution is estimated at 0.083 for body B_{1a} and 0.033 for B_{1b} .

Fig. 10 shows that the axial force, $-C_x$, increases with increasing incidence, becoming about 50% higher than its zero incidence value by 20° incidence. However this large change in $-C_x$ is not so significant when the drag coefficient C_D related to stability axes is considered. Thus if, at 20° incidence, $-C_x$ was assumed equal to its zero incidence value, the error in C_D would amount to only about 5%.

4.2 Wing and body

4.2.1 Longitudinal and drag characteristics

C_Z and C_m for the various wing-body combinations are shown in Figs. 6 and 7 plotted against incidence. Only the values at zero sideslip are presented, as it was found that sideslip angles up to 10° had a negligible effect on these coefficients. It is seen that $-C_Z$ and C_m become non-linear only above about 10° incidence, and that, even at 20° incidence, the magnitude of the non-linearity amounts to only about 10% or less. Because C_Z is based on body cross-sectional area, $-C_Z$ decreases with increasing wing aspect ratio. If C_Z were based on exposed wing area the reverse would be true, the values of $-\frac{dC_Z}{da}$ at low incidence, for example, being 1.32, 1.42, and 1.51 for W_1B_{1a} , W_2B_{1a} and W_3B_{1a} respectively. Increasing the fineness ratio of the nose has little effect on C_Z but increases the stability slightly. The centre of pressure variation with incidence is small for all configurations, the smallest variation being with wing W_1 (Fig. 8). The centre of pressure is very close to the centroid of the plan area for W_1B_{1a} and W_1B_{1b} , but is up to $\frac{1}{2}d$ further aft than the centroid for W_2B_{1a} and W_3B_{1a} .

Comparison of experiment with theoretical predictions for the low incidence characteristics gives the following:

	W_1B_{1a}		W_1B_{1b}		W_2B_{1a}		W_3B_{1a}	
	Exp.	Theory	Exp.	Theory	Exp.	Theory	Exp.	Theory
$-\frac{dC_Z}{da}$	32.6	32.4	32.8	32.4	28.0	29.7	24.8	25.8
\bar{x}/d	8.8	9.0	8.9	9.1	9.3	9.5	9.6	9.8

The theoretical values given were derived using the linear theory of Ref. 6 for the wing alone, Ref. 3 for the body and Ref. 7 for the wing-body interference factors. Agreement between theory and experiment is seen to be good, the largest error in $\frac{dC_Z}{da}$ occurring with the wing which has a sonic leading edge (W_2) and amounting to 6%. This is well within the $\pm 10\%$ claimed for the method⁷. The estimated centre of pressure position is 0.2d behind the measured position for all configurations. This is consistent with Ref. 7 where comparison with experiment showed the estimated values to be generally too far aft by about 0.009 body lengthn (0.12d). As C_Z and C_m are reasonably linear with incidence, (Figs. 6 and 7), the calculated slopes at low incidence can be used to give a good measure of these quantities up to 20° incidence.

The zero-lift drag variation with Reynolds number is shown in Fig. 9. The 'estimated' curves shown were obtained by calculating a skin friction drag⁵ for wholly turbulent flow and adding a wave drag

contribution, invariant with Reynolds number, to give a best fit with the experimental data. It is seen that the trend of the results is consistent with this assumption of wholly turbulent flow, bearing in mind the larger experimental errors at the lower Reynolds numbers (para. 3.2). The wing-body wave drags so obtained are tabulated below together with the body alone values (para. 4.1). Also given are the wing contributions assuming that wing and body wave drags are additive.

	Wing-body wave drag	Body alone wave drag	Wing wave drag = (W + B) - B
$B_{1a} W_1$	0.100	0.083	0.017
$B_{1b} W_1$	0.056	0.033	0.023
$B_{1a} W_2$	0.117	0.083	0.034
$B_{1a} W_3$	0.115	0.083	0.032

Of the theoretical methods available for calculating wing or wing-body wave drags, only Randall's method¹⁴ is applicable to wings with sonic or near sonic leading edges. However as both the possible experimental errors and the errors in the estimation of skin friction drag are of about the same magnitude as the measured wing wave drag contribution, a comparison with this theory has not been felt to be particularly helpful and has therefore not been made.

The increase in axial force with incidence is shown in Fig. 10 for each configuration at zero sideslip and maximum Reynolds number (32×10^6). At 20° incidence, the axial force has increased by about 50% of its value at zero incidence. However, as was pointed out for the body alone results (para 4.1), this large change in $-C_X$ corresponds to only a small change (about 2 or 3%) in the value of C_D at 20° incidence, where C_D is the drag coefficient related to stability axes. Hence good estimates of C_D can be made by assuming that $-C_X$ is invariant with incidence.

The effect of sideslip angle on the zero lift axial force is shown in Fig. 11. At 10° sideslip the axial force has increased by about 0.04, or 20%. As the corresponding value for the body alone (Fig. 10) is about 0.015, the increase in wave drag of the yawed wings is evidently quite significant. The increase in $-C_X$ with sideslip was found to become less as incidence increased, so that at 20° incidence the increment in C_X had fallen from 0.04 to 0.025.

Lift-drag ratios calculated for stability axes are shown in Fig. 12 for a Reynolds number of 32×10^6 . Maximum L/D occurs at about 5° incidence for all wing-body combinations, the wing of smallest aspect ratio giving the highest L/D viz. 5.7. This value is increased to 6.2 by fitting the more slender nose. These values of L/D are considered to be reasonably representative of full scale, as a Reynolds number of 32×10^6 corresponds to full scale conditions at 68,000 ft altitude on a vehicle 4 times model size.

4.2.2 Lateral and directional characteristics

Figs. 13, 14 and 15 show the side force and yawing moment derivatives, C_Y and C_n , and the side-force centre of pressure position plotted against incidence for sideslip angles of 5° and 10° . Also shown are the body-alone

values as derived from the measured body normal force and pitching moment. Thus the effective incidence, σ , of the body due to combined incidence α and sideslip β is given by

$$\sin\sigma = \cos\alpha (\tan^2\alpha + \sin^2\beta)^{\frac{1}{2}}$$

and if $-C_z$ and C_m are the body normal force and pitching moment at incidence σ

$$C_Y = C_z \sin\beta / \sin\sigma$$

$$C_n = -C_m \sin\beta / \sin\sigma$$

As the wings are centrally positioned on the body, little interference between the wing and body might be expected at zero incidence, and this is seen to be the case for all configurations, the measured C_Y and C_n being in excellent agreement with the body alone values. This agreement in fact continues to be good over the full incidence range for configurations W_2B_{1a} and W_3B_{1a} . However the larger chord wing on configurations W_1B_{1a} and W_1B_{1b} seems to prevent the lateral force on the rear of the body from developing to its full extent and, in consequence, as incidence increases, $-C_Y$ becomes smaller than the body alone values and the side-force centre-of-pressure does not move so far aft. The magnitude of this wing interference is many times smaller than would be predicted by the method of Ref. 8. In this reference, the assumption is made that the wing inhibits body viscous cross flow due to incidence along a body length equal to the wing root chord: hence over this region the side force and yawing moment arise only from β and not from the resolved components due to combined α and β . The experimental results of Figs. 13-15 show no such inhibition of the body viscous cross flow for wings W_2 and W_3 and only a relatively small effect from wing W_1 .

The induced rolling moment due to sideslip is shown in Fig. 16. It is seen that the rate of change of rolling moment with incidence decreases progressively with increasing incidence, approaching zero for all configurations at about 20° incidence.

For all the wings tested, the sweep of the leading edge of the forward wing is less than the sweep of the Mach line at $\beta = 5^\circ$ and above* Wing-alone theory¹¹ shows that $-\frac{dC}{d\alpha} \frac{\ell}{c}$ at $\alpha = 0$ and constant β begins to decrease rapidly as the leading edge of one panel becomes supersonic, and it would thus be expected that estimates based on slender body theory would give values of $-\frac{dC}{d\alpha} \frac{\ell}{c}$ that are too high. The table below shows this to be the case, the values estimated from Refs. 9 and 10 being up to twice as high as the experimental values. Although no method is available for calculating the induced rolling moment on a non-slender wing-body combination, Ref. 11 gives a method for the wing alone. If it is assumed that the wing-body interference factor is the same as for

* Schlieren shows that, although the leading edge of one panel of wing 1 is ahead of the Mach line, the bow shock is in fact still detached at both $\beta = 5^\circ$ and 10° .

slender wings¹⁰, then the estimates shown in the last columns are obtained. Although the agreement with experiment is good in some cases, it is not consistently so.

	$-\frac{dC_l}{d\alpha}(\alpha=0)$							
	Experiment		Slender-body theory				Wing alone values of Ref. 11 + body interference from Ref. 10	
			Reference 9		Reference 10			
	$\beta = 5^\circ$	$\beta = 10^\circ$	$\beta = 5^\circ$	$\beta = 10^\circ$	$\beta = 5^\circ$	$\beta = 10^\circ$	$\beta = 5^\circ$	$\beta = 10^\circ$
W_1B_{1a}	4.3	10.3	8.5	15.4	10.2	20.4	7.6	11.6
W_2B_{1a}	3.3	6.3	6.1	11.4	7.4	14.6	3.2	6.1
W_3B_{1a}	2.9	5.5	4.4	8.3	5.4	10.8	1.0	3.2

4.2.3 Flow field around models

Schlieren photographs were taken of the models at zero sideslip at various incidences, and typical photographs are shown in Fig. 17. The distances from the horizontal plane of symmetry to the body and wing shock waves and to the body vertices were measured from these photographs and the results are shown in Figs. 18(a) and (b) for two longitudinal stations, one at the body trailing edge and the other at 3d upstream from this. It was found that the locations of the body bow shock agreed so well with the predictions from the semi-empirical theory of Refs. 12 and 13 that it was not found possible to distinguish between the experimental and predicted curves in Fig. 18.

For a monostable missile whose incidence variations are predominantly positive, a ramjet-engine-intake position can clearly be found below the body such that the body and wing shocks never enter the intake. However, if the missile is to be bistable and hence have equal and large positive and negative incidence ranges, Fig. 18 suggests that there will be a problem in locating a rear-mounted intake so as to avoid the wing and body shocks and yet be clear of the low stagnation pressure and low Mach number region associated with the body vortices.

In further tests with these models, it is intended to make a survey of the local Mach number, stagnation pressure, and flow angularity around the models so as to determine suitable engine intake locations.

5 FURTHER WORK

The models which form the basis of this report have also been tested in the 8 ft tunnel over the Mach number range from 1.3 to 2.8, and the results are being analysed.

The next series of tests in the H.S.S.T. will be

- (i) flow surveys above and below body to determine suitable intake positions,
- (ii) flow surveys behind wings in region occupied by controls on $B_{1a}W_1$,
- (iii) control effectiveness studies on $B_{1a}W_1$.

The complete programme of work for the H.S.S.T. and 8 ft tunnels is detailed in Ref. 1.

6 CONCLUSIONS

Tests have been made at a Mach number of 4 on two bodies of circular cross section and of fineness ratio 13, having ogival noses of length 3d and 5d respectively, and on these bodies combined with delta wings of aspect ratios 0.83, 1.03 and 1.24. The wing span of all combinations was 5d. The main results from these tests and from comparisons with theory are as follows:

- (1) The normal force and pitching moment for all wing-body combinations tested is reasonably linear up to 20° incidence, and the centre of pressure position moves by only about $\frac{1}{4}d$ or less over this incidence range. The smallest centre of pressure movement is with the wing of smallest aspect ratio (i.e. largest root chord).
- (2) Calculated values of normal force and centre of pressure position near zero lift agree well with experiment, and, because of the small non-linearities, give a good approximation to the experimental values over the whole incidence range.
- (3) Maximum lift-drag ratio occurs at about 5° incidence and is largest for the wing of smallest aspect ratio, this arrangement giving 5.7 with the 3d nose and 6.2 with the 5d ogival nose.
- (4) At zero incidence, the side force and yawing moments for the wing-body combinations are in excellent agreement with values obtained from the body alone normal force and pitching moment, assuming no wing interference. This agreement continues to be good over the full incidence range for the smaller chord wings, but the wing of largest root chord (i.e. smallest aspect ratio) seems to prevent the lateral force on the rear of the body from developing to its full extent.
- (5) No satisfactory method exists for predicting the rolling moment due to sideslip for wing-body combinations where the wing leading edge is sonic or near sonic.
- (6) The body alone normal force, centre of pressure position, and zero lift drag can be adequately predicted from existing methods.

LIST OF SYMBOLS

Unless otherwise stated, the body axes system shown in Fig. 1 has been used throughout. All moments are referred to a position at $7.604d$ from the body vertex.

C_D	drag coefficient (stability axes (Fig. 1))	$\frac{\text{Drag}}{q \frac{\pi}{4} d^2}$
C_ℓ	rolling moment coefficient	$\frac{\text{Rolling moment}}{q \frac{\pi}{4} d^3}$
$\frac{dC_\ell}{d\alpha} (\alpha=0)$	slope of rolling moment coefficient versus incidence at $\alpha = 0$ and constant β (per radian)	
C_m	pitching moment coefficient	$\frac{\text{P.Mt.}}{q \frac{\pi}{4} d^3}$
$\frac{dC_m}{d\alpha}$	pitching moment coefficient slope for angle of incidence (per radian)	
C_m	yawing moment coefficient	$\frac{\text{Y.Mt.}}{q \frac{\pi}{4} d^3}$
$-C_X$	axial force coefficient	$\frac{\text{Axial force}}{q \frac{\pi}{4} d^2}$
C_Y	side force coefficient	$\frac{\text{Side force}}{q \frac{\pi}{4} d^2}$
$-C_Z$	normal force coefficient	$\frac{\text{Normal force}}{q \frac{\pi}{4} d^2}$
$\frac{dC_Z}{d\alpha}$	normal force coefficient slope for angle of incidence (per radian)	
d	body diameter	
h	height above or below body centreline measured in body diameters	
L/D	lift/drag ratio for stability axes (Fig. 1)	
M	free stream Mach number	
q	free stream dynamic pressure	
r	radius of nose at distance x from body vertex	
R	free stream Reynolds number based on body overall length	
x, y, z	reference axes. For body axes, these are forward along the body axis, normal to the body and to starboard, and normal to the body and downwards, respectively.	
\bar{x}	distance from body vertex to centre of pressure position	

LIST OF SYMBOLS (Contd)

α	angle of incidence (degrees) [$\alpha = \tan^{-1} (\tan\sigma \cos\lambda)$]
β	sideslip angle (degrees) [$\beta = \sin^{-1} (\sin\sigma \sin\lambda)$]
σ	angle between body axis and wind vector
λ	angle between plane containing body axis and z axis and plane containing body axis and wind vector
ϕ	wing leading edge sweepback angle.


LIST OF REFERENCES

<u>No.</u>	<u>Author</u>	<u>Title etc.</u>
1	Winter, K.G., Lawlor, E.F., Andrews, D.R.	Unpublished M.O.A. Report.
2	Moss, G.F. Payne, D.G.	A compact design of six component internal strain gauge balance. R.A.E. Tech. Note Aero 2764 July, 1961
3	Syvertson, C.A., Dennis, D.H.	A second-order shock-expansion method applicable to bodies of revolution near zero lift. NACA Report 1328 1957
4	-	Data sheets. Aerodynamics Vols. I and II. Royal Aeronautical Society. October, 1960
5	Monaghan, R.J.	Formulae and approximations for aerodynamic heating rates in high speed flight. A.R.C. CP.360 October, 1955
6	Stanbrock, A.	The lift curve slope and aerodynamic centre position of wings at subsonic and supersonic speeds. R.A.E. Tech. Note Aero 2328 November, 1954 A.R.C. 17615
7	Pitts, W.C., Nielson, J.N., Kaattari, G.E.	Lift and center of pressure of wing-body-tail combinations at subsonic, transonic and supersonic speeds. NACA Report 1307 1957
8	Kaattari, G.E.	Estimation of directional stability derivatives at moderate angles and supersonic speeds. NASA Memo. 12-1-58A (TIL.6349) January, 1959
9	Collingburne, J.R.	Unpublished M.O.A. Report.
10	Spahr, J.R.	Contribution of the wing panels to the forces and moments of supersonic wing-body combinations at combined angles. NACA T.N. 4146 January, 1958

LIST OF REFERENCES (Contd)

<u>No.</u>	<u>Author</u>	<u>Title etc.</u>
11	Jones, A.L., Alksne, A.	A summary of lateral stability derivatives calculated for wing plan forms in supersonic flow. NACA Report 1052 1951
12	Love, E.S., Long, R.H.	A rapid method for predicting attached shock shape. NACA T.N. 4167 October, 1957
13	Hill, W.A. Jr.	Force, moment, and flow-field characteristics of two wing-body-nacelle combinations at Mach numbers of 2 and 3. NASA T.M. X-3 January, 1960
14	Randall, D.G.	A technique for improving the predictions of linearised theory on the drag of straight edged-wings. A.R.C. CP.394 January, 1957

TABLE 1
Details of bodies and wings tested

Body	Cross-sectional shape	Size	Overall length		Nose length		Nose shape
			Units of d	Inches	Units of d	Inches	
B _{1a}	Circular 	$d = 3.70$ in.	13	48.107	3	11.10	Ogive $\frac{r}{d} = -0.002615 \left(\frac{x}{d}\right)^3 - 0.039667 \left(\frac{x}{d}\right)^2 + 0.30984 \left(\frac{x}{d}\right)$
B _{1b}	"	$d = 3.70$ in.	13	48.107	5	18.50	Ogive $\frac{r}{d} = -0.000308 \left(\frac{x}{d}\right)^3 - 0.016924 \left(\frac{x}{d}\right)^2 + 0.19231 \left(\frac{x}{d}\right)$

Wing	Planform	Cross span		Root chord		Distance from wing root TE to body end		Wing thickness (inches)	Wing LE included angle (measured normal to LE)	Wing TE included angle (measured normal to TE)	Wing LE semi vertex Angle (nominal)
		Units of d (nominal)	Inches (measured)	Units of d (nominal)	Inches (measured)	nominal	Inches (measured)				
W ₁	Delta	5	18.450	9.6825	33.792	0	0.039	0.501	15.3°	15.1°	11.67°
W ₂	"	5	18.457	7.7460	28.530	0	0.030	0.501	15.2°	15.2°	14.48°
W ₃	"	5	18.399	6.4550	23.750	0	0.038	0.479	15.3°	15.1°	17.22°

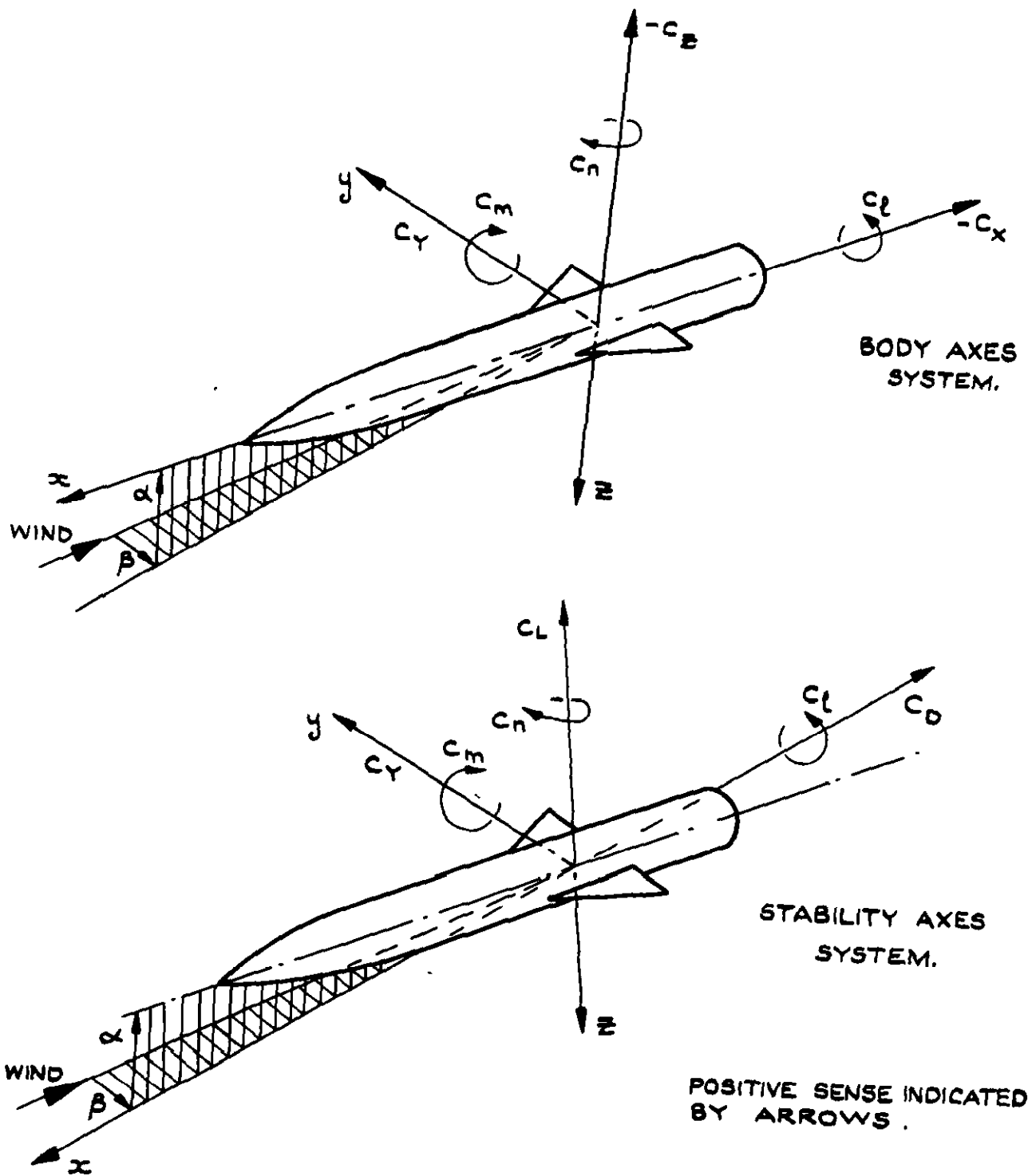
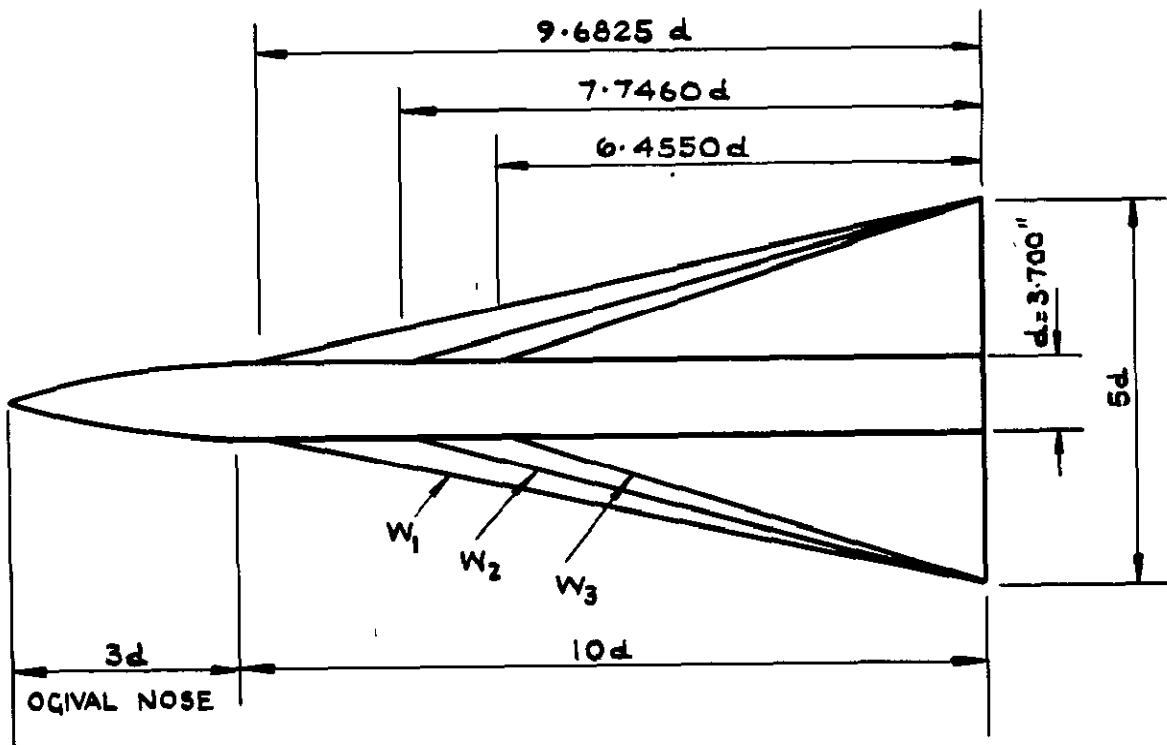
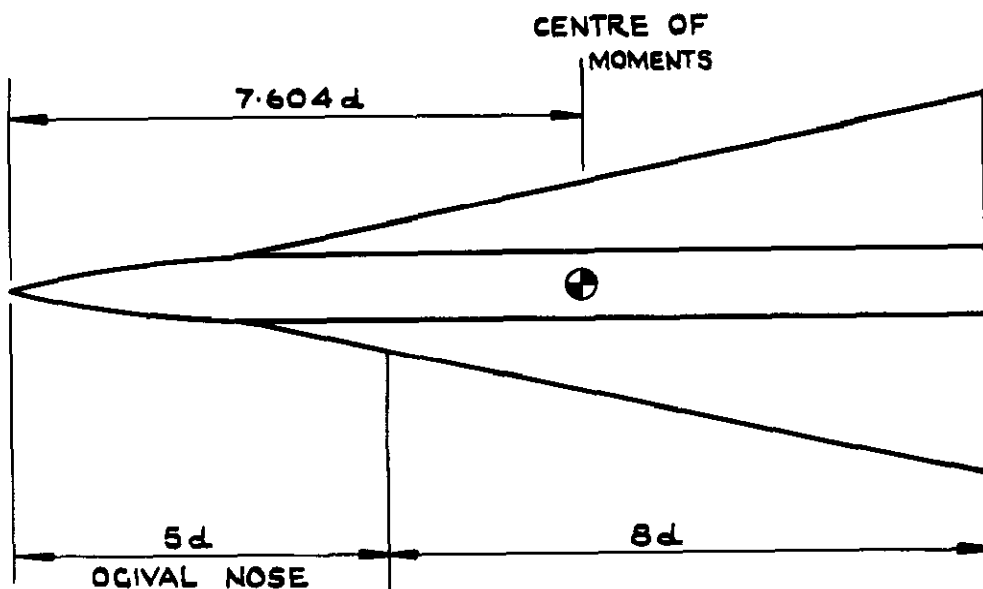


FIG. I. FORCE AND MOMENT REFERENCE AXES.



WINGS W_1 , W_2 , OR W_3 ON BODY B_{1a} .



WING W_1 ON BODY B_{1b} .

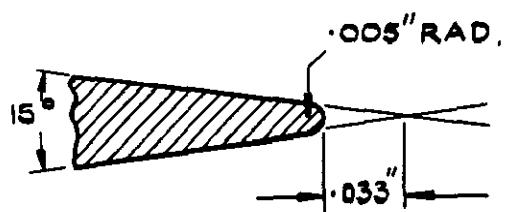
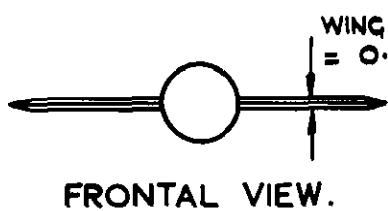


FIG. 2. MODEL CONFIGURATIONS TESTED.

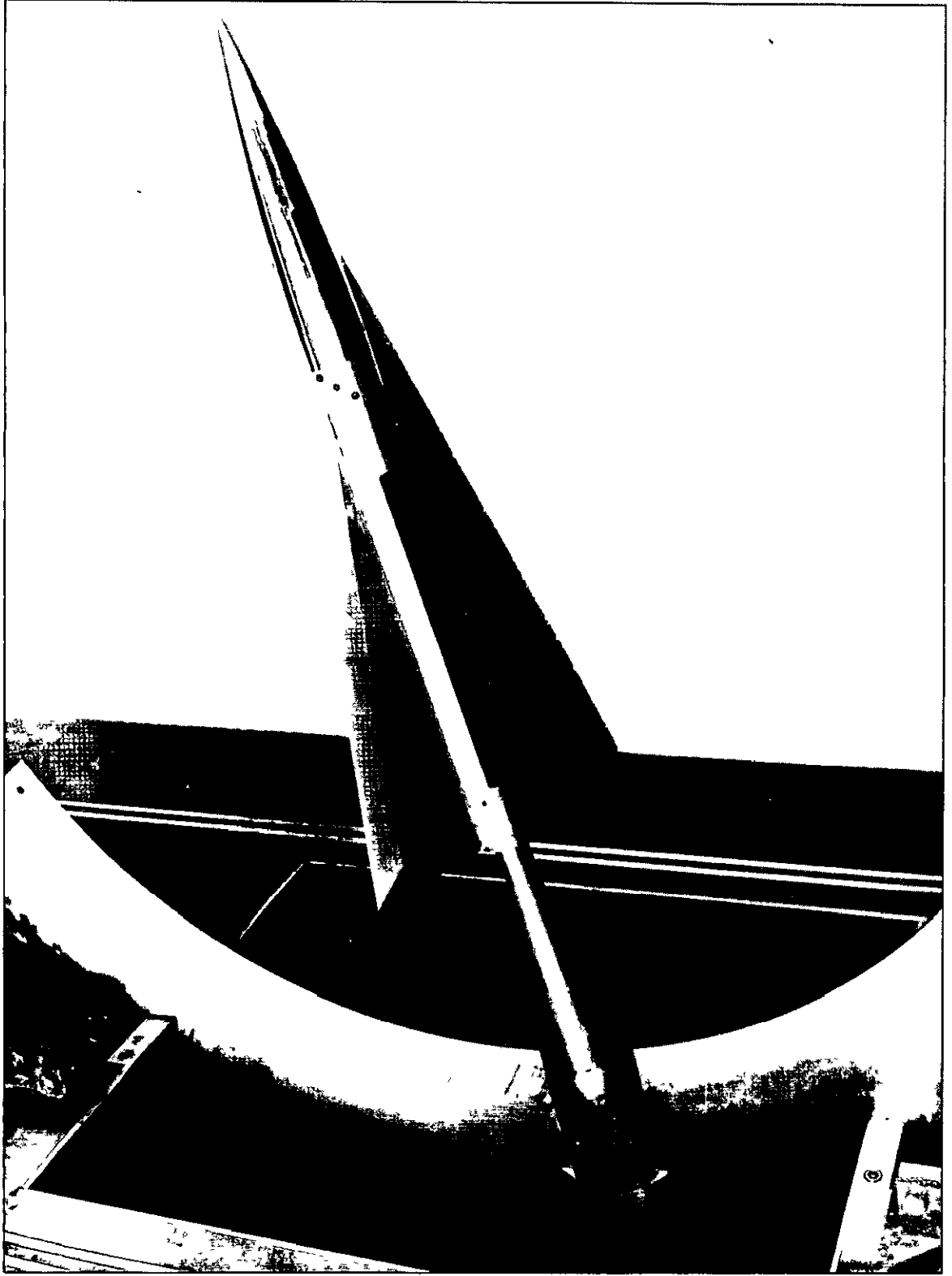


FIG 3. CONFIGURATION B_{1b}W₁ MOUNTED IN THE TUNNEL

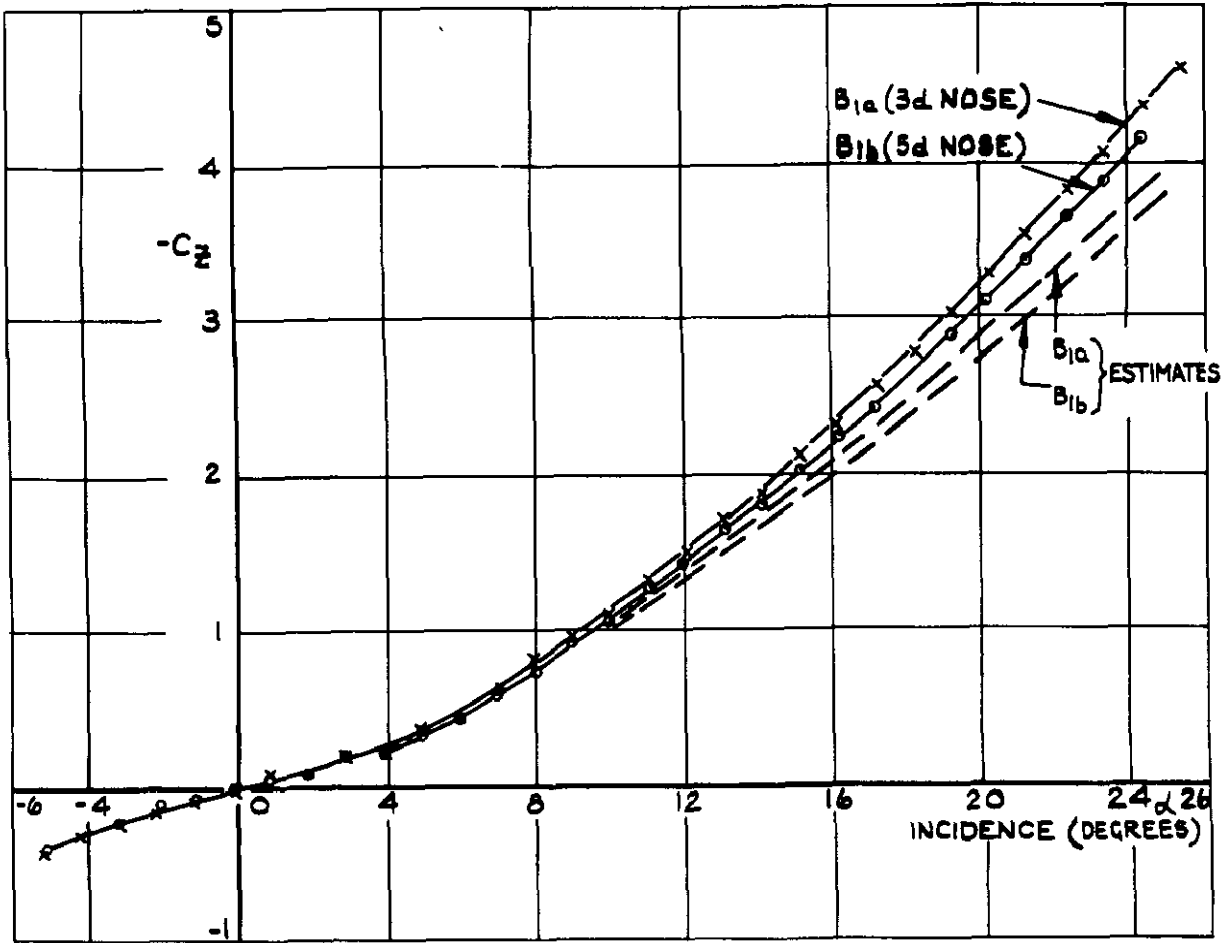


FIG. 4. NORMAL FORCE COEFFICIENT FOR BODY ALONE.

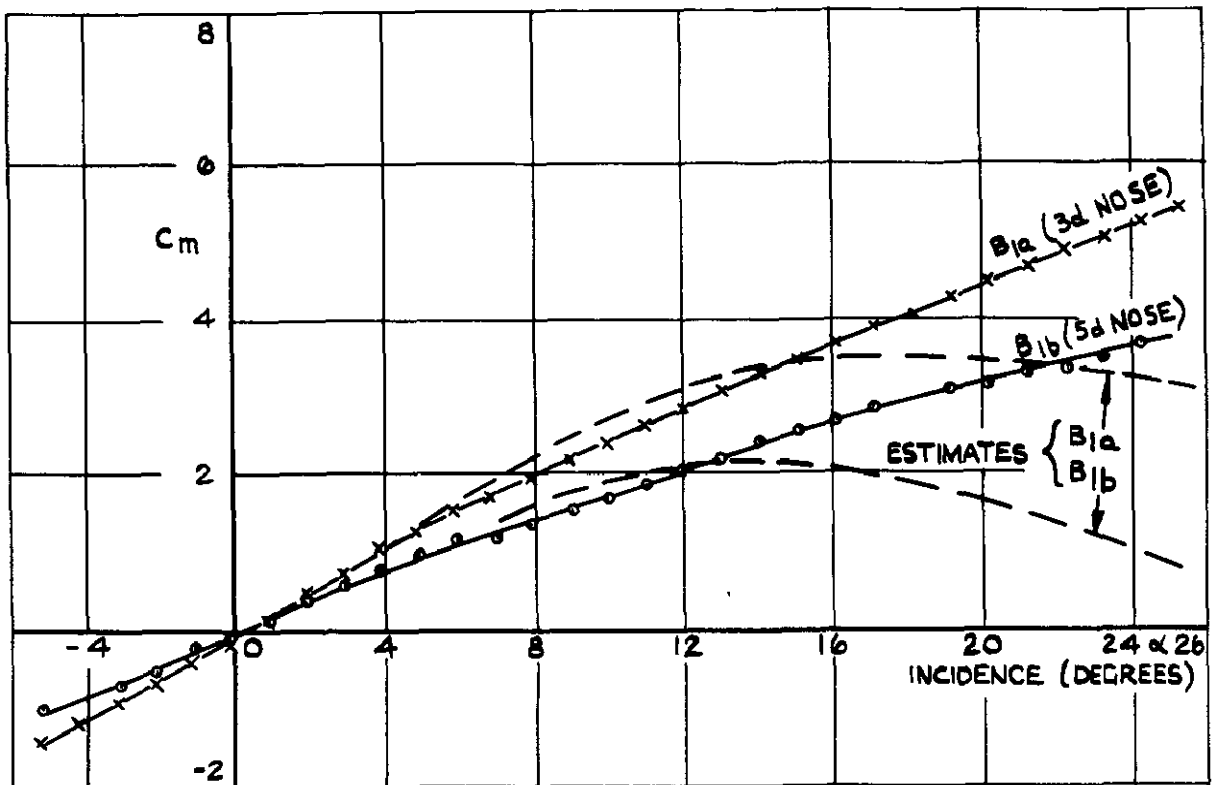


FIG. 5. PITCHING MOMENT COEFFICIENT FOR BODY ALONE.

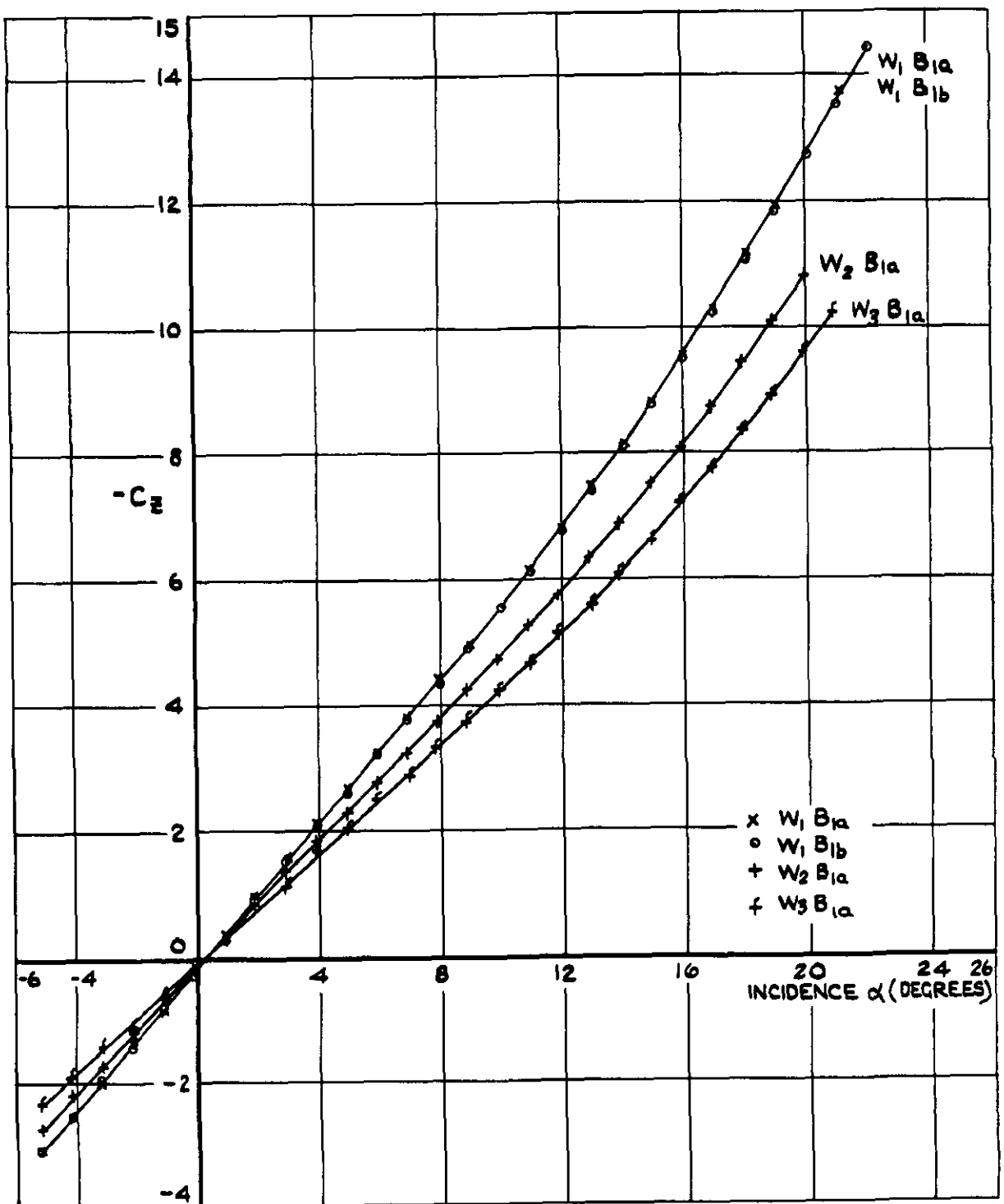


FIG.6. NORMAL FORCE COEFFICIENT VERSUS INCIDENCE FOR WING-BODY CONFIGURATIONS AT ZERO SIDESLIP.

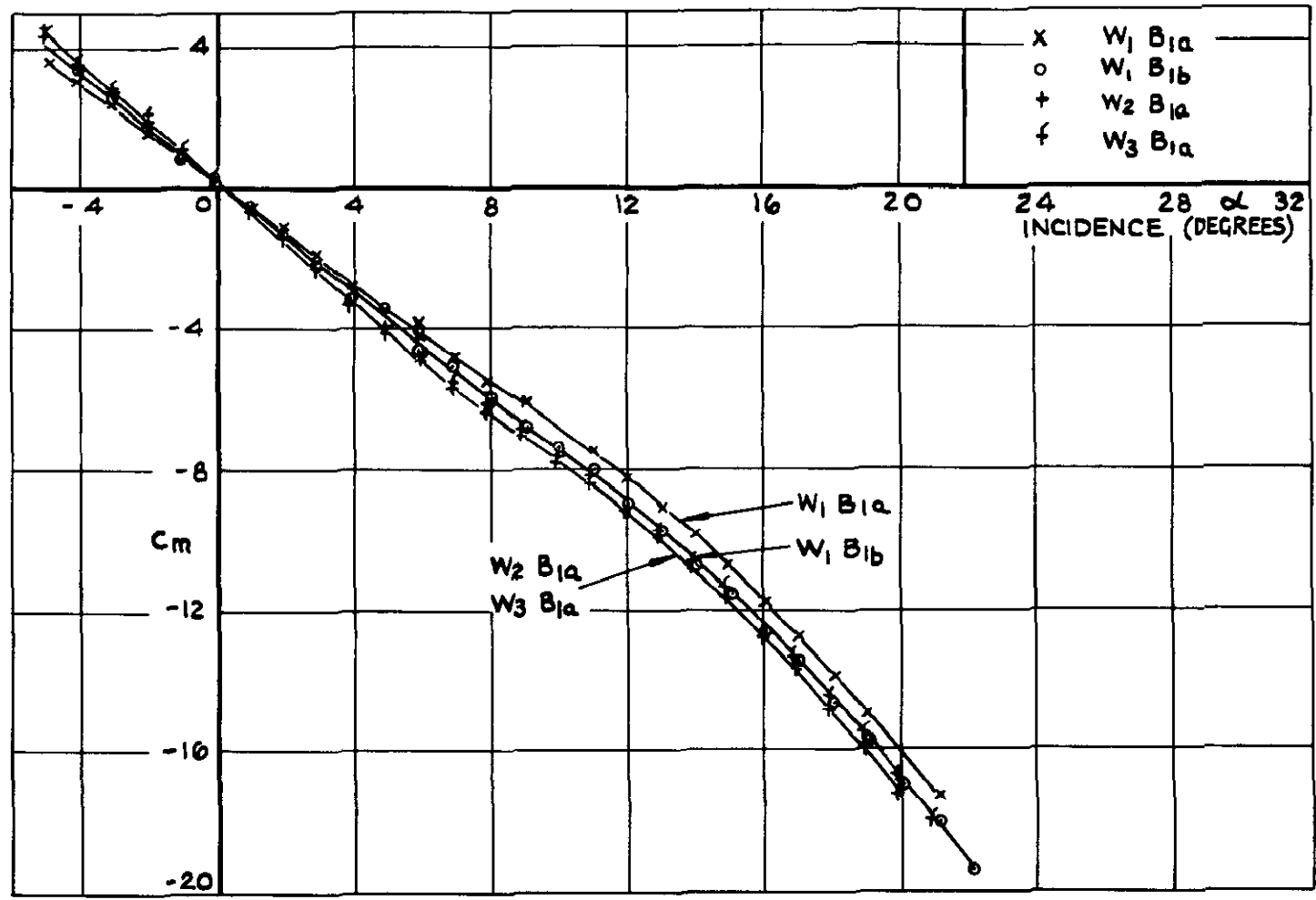


FIG.7, PITCHING MOMENT COEFFICIENT VERSUS INCIDENCE FOR WING-BODY CONFIGURATIONS A ZERO SIDESLIP.

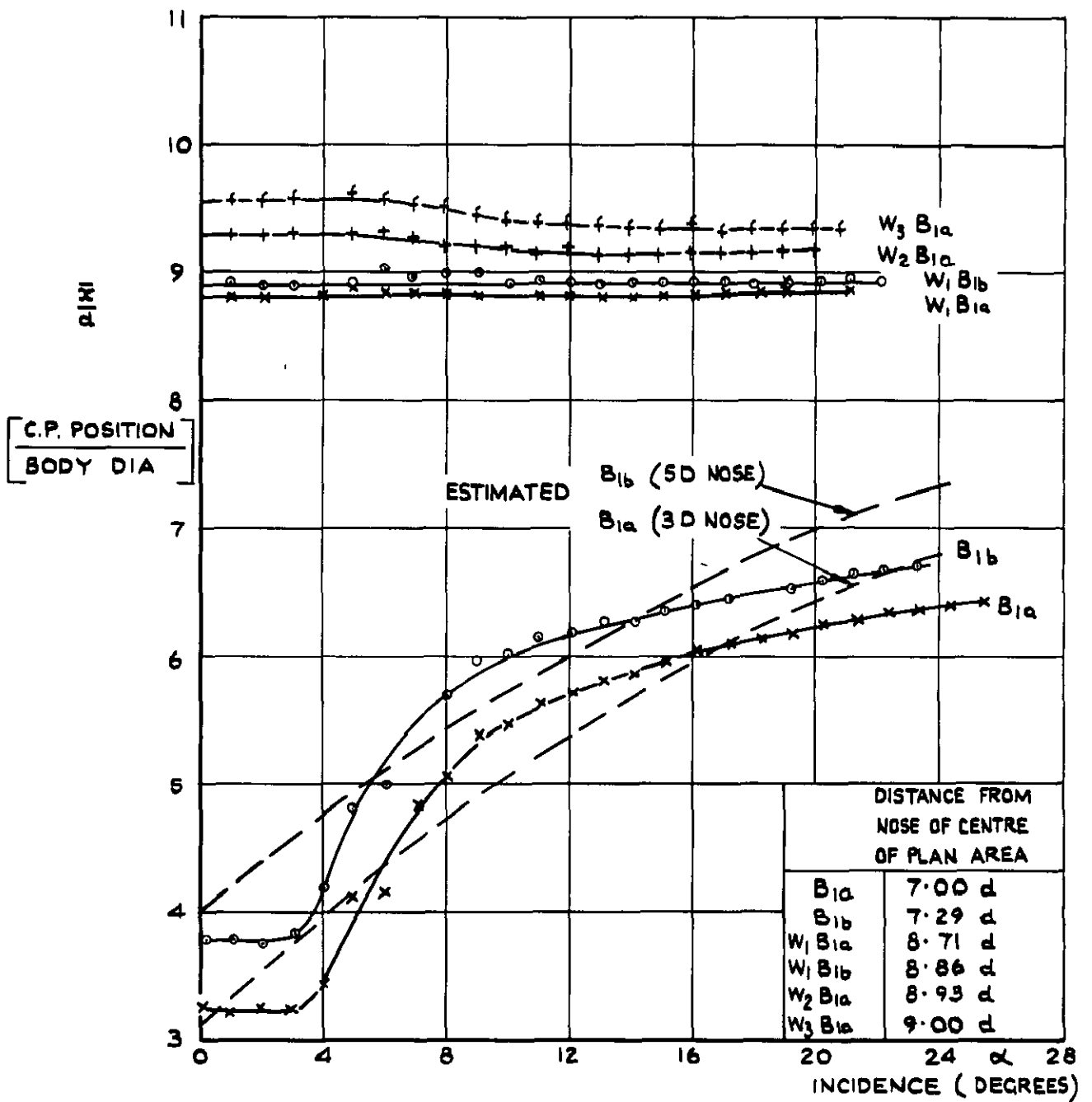
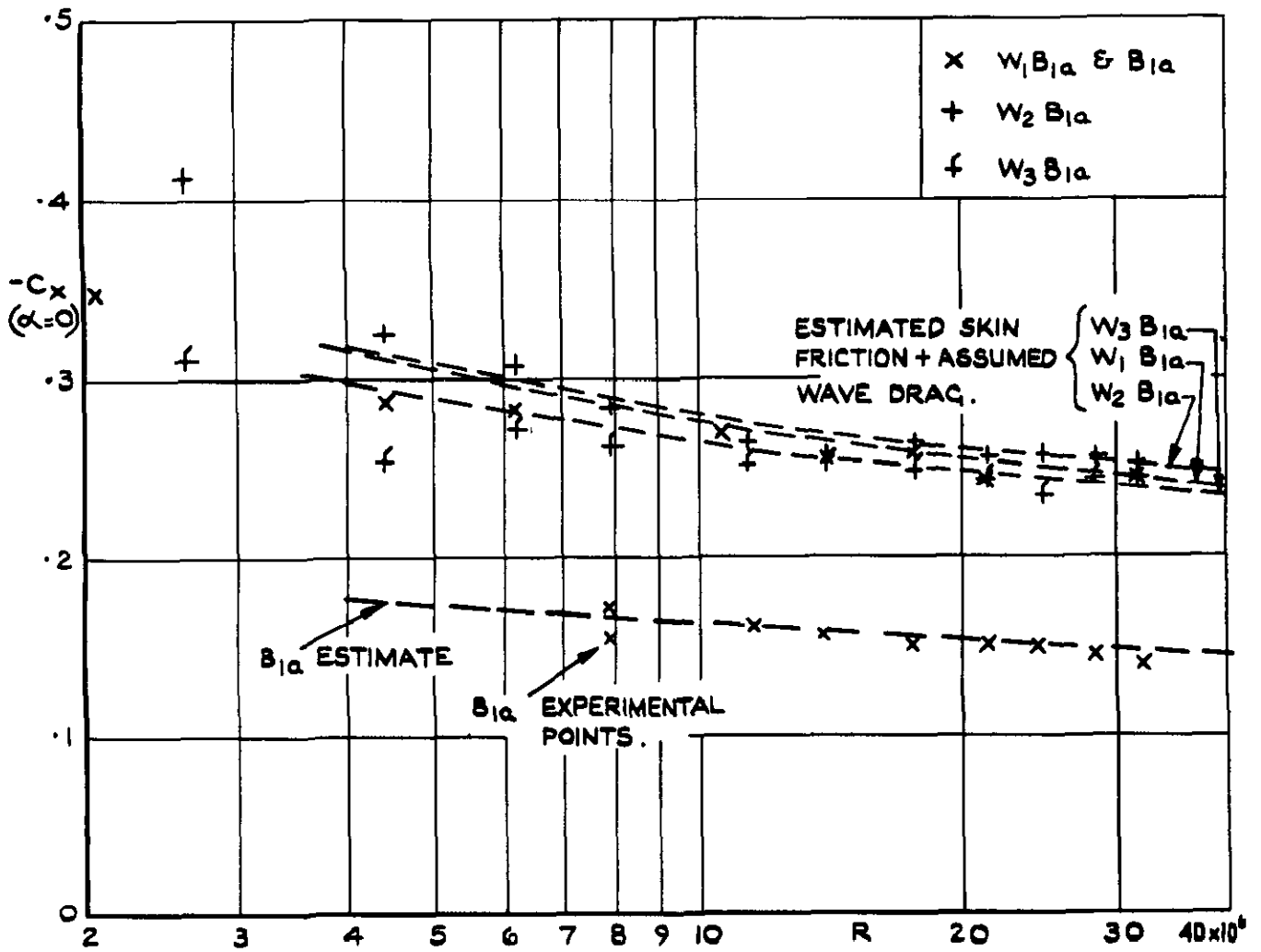
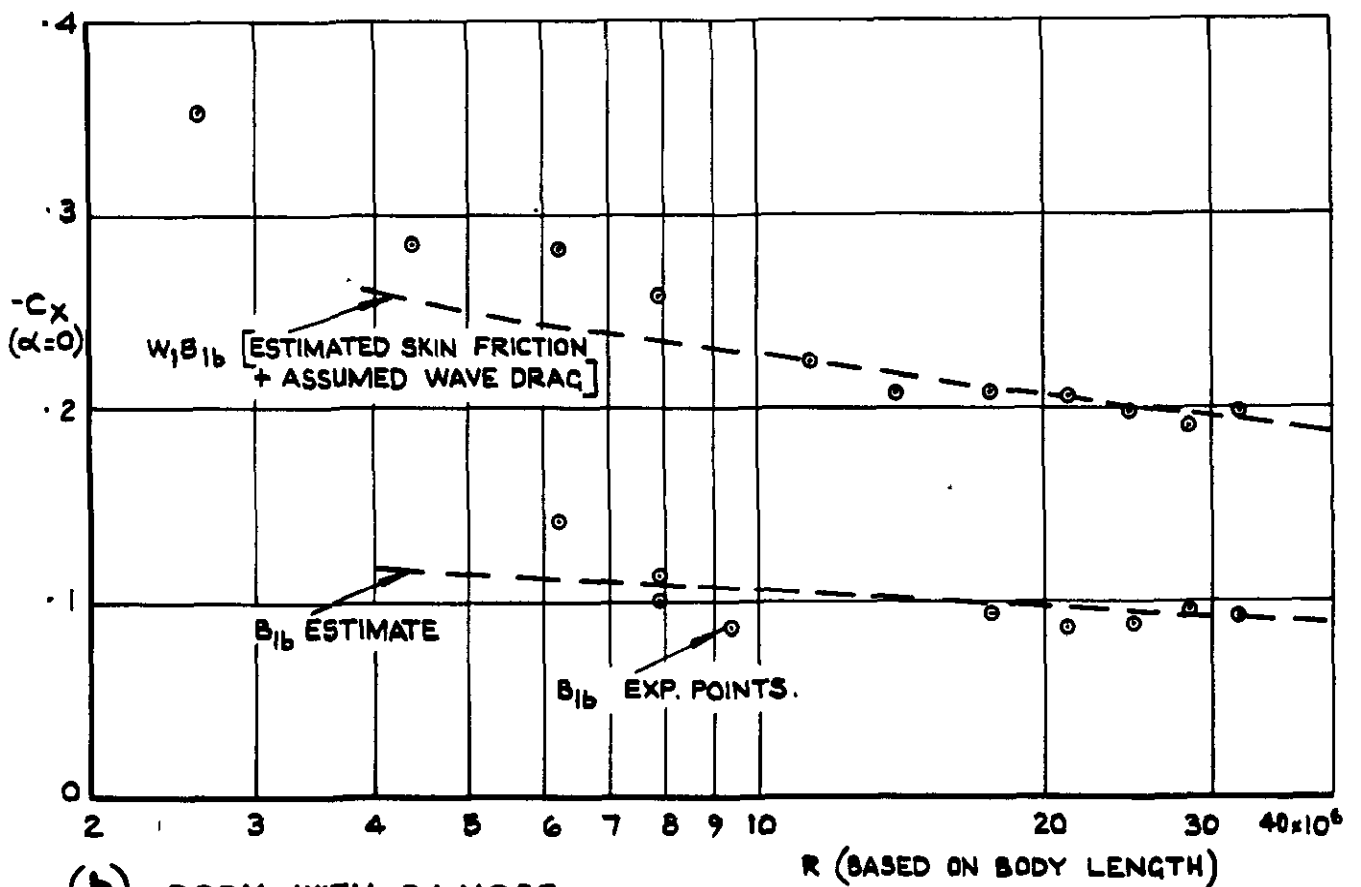


FIG. 8. CENTRE OF PRESSURE POSITION MEASURED FROM BODY VERTEX.



(a) BODY WITH 3d NOSE.



(b) BODY WITH 5d NOSE.

FIG. 9. EFFECT OF REYNOLDS NUMBER ON ZERO-LIFT DRAG.

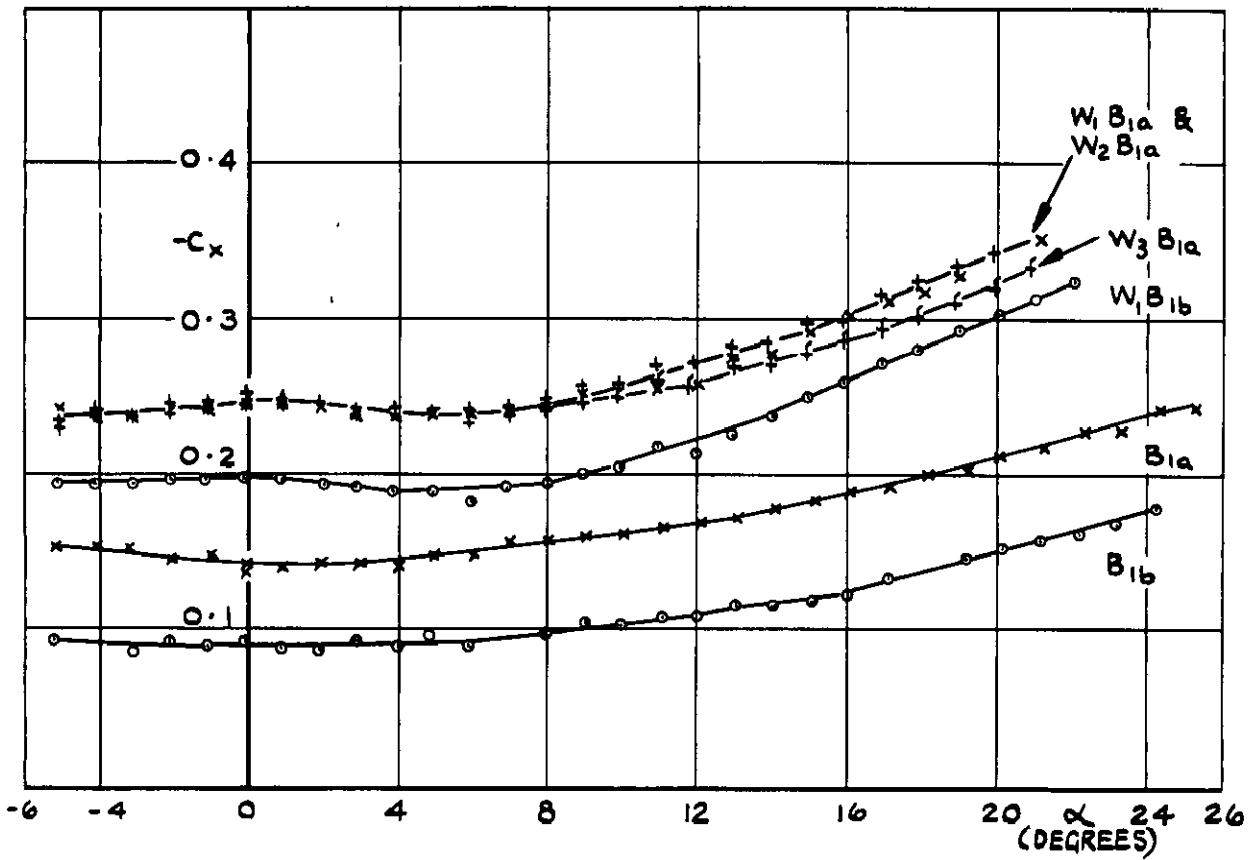


FIG. 10. AXIAL FORCE VARIATION WITH INCIDENCE
 $(R = 32 \times 10^6)$

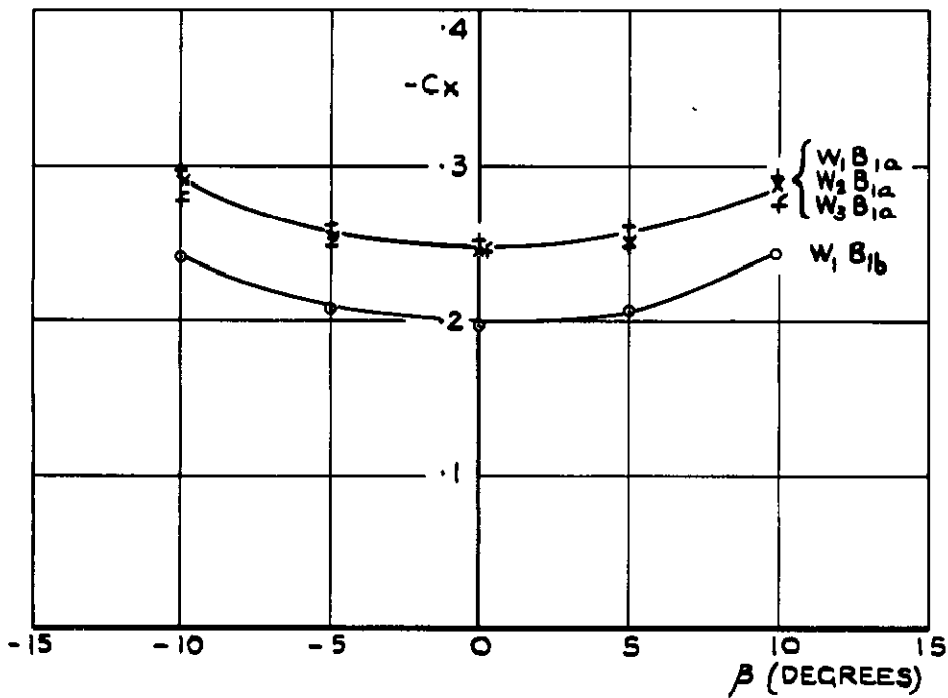


FIG. 11. EFFECT OF SIDESLIP ON AXIAL FORCE
 AT ZERO LIFT. $(R = 32 \times 10^6)$

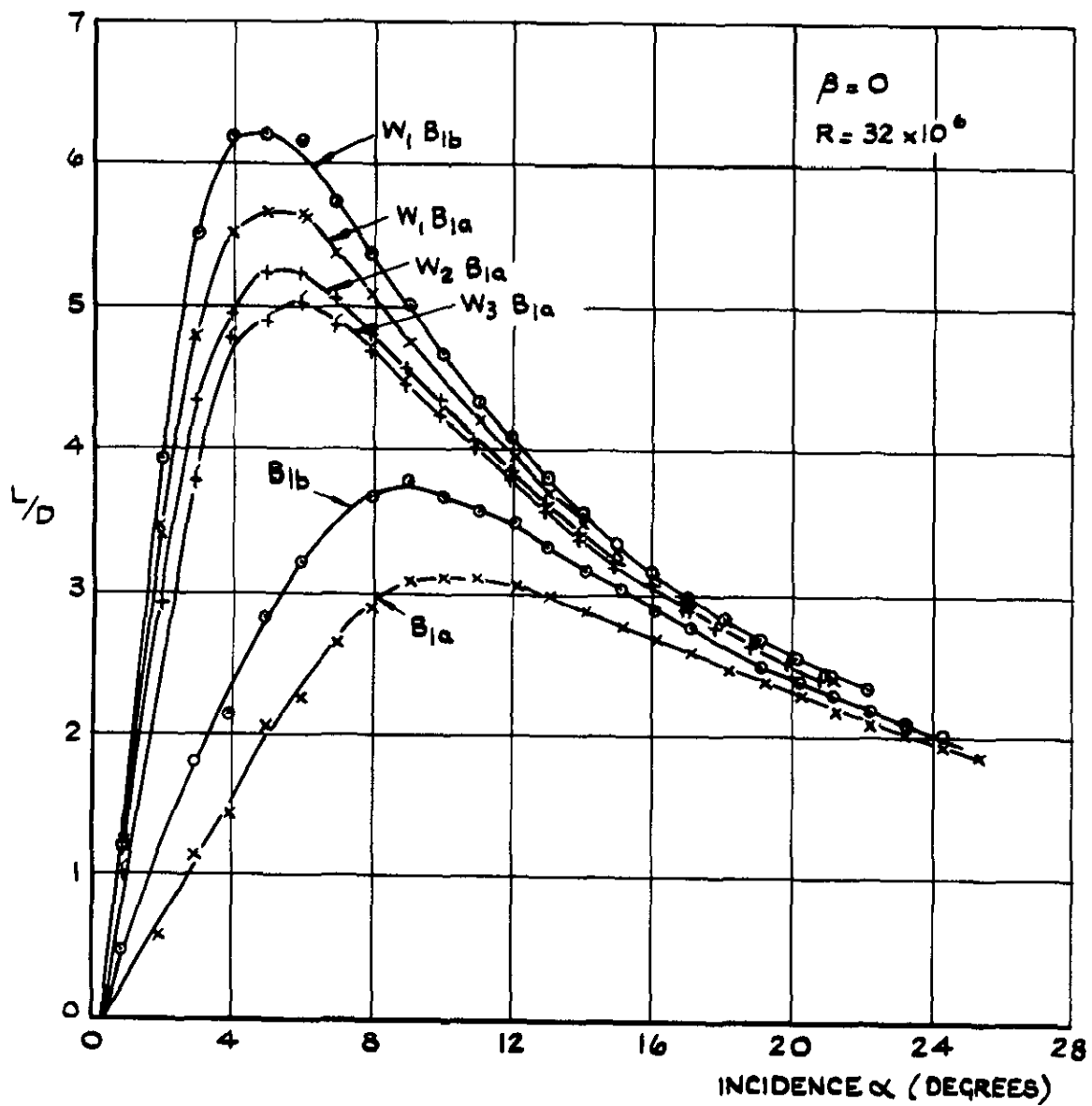


FIG. 12. LIFT TO DRAG RATIOS.

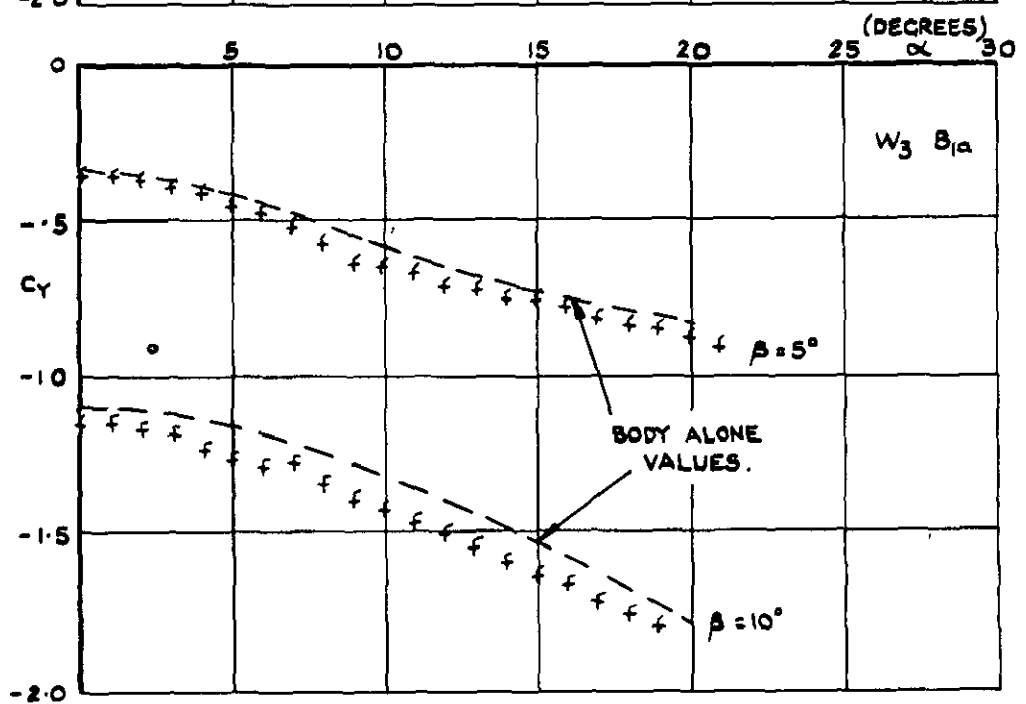
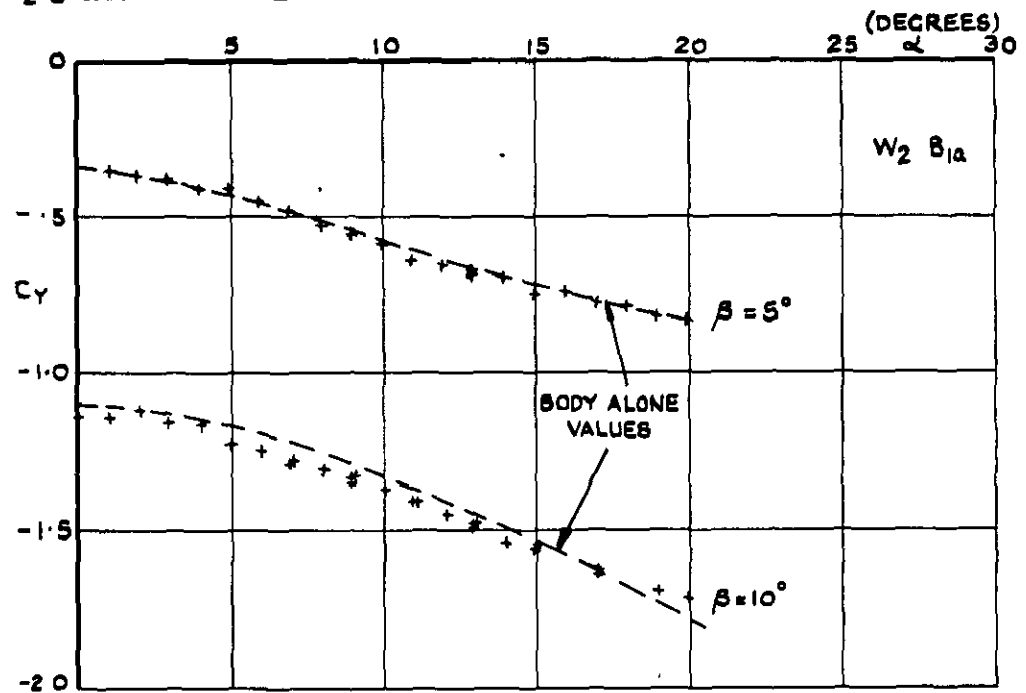
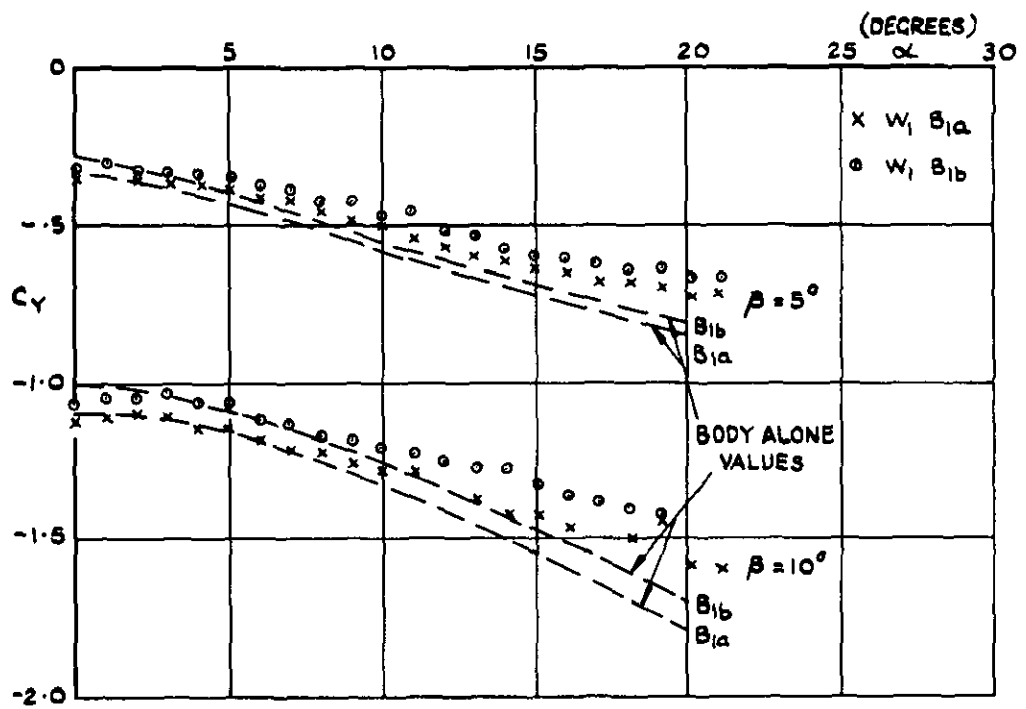


FIG. 13. SIDE FORCE COEFFICIENT.

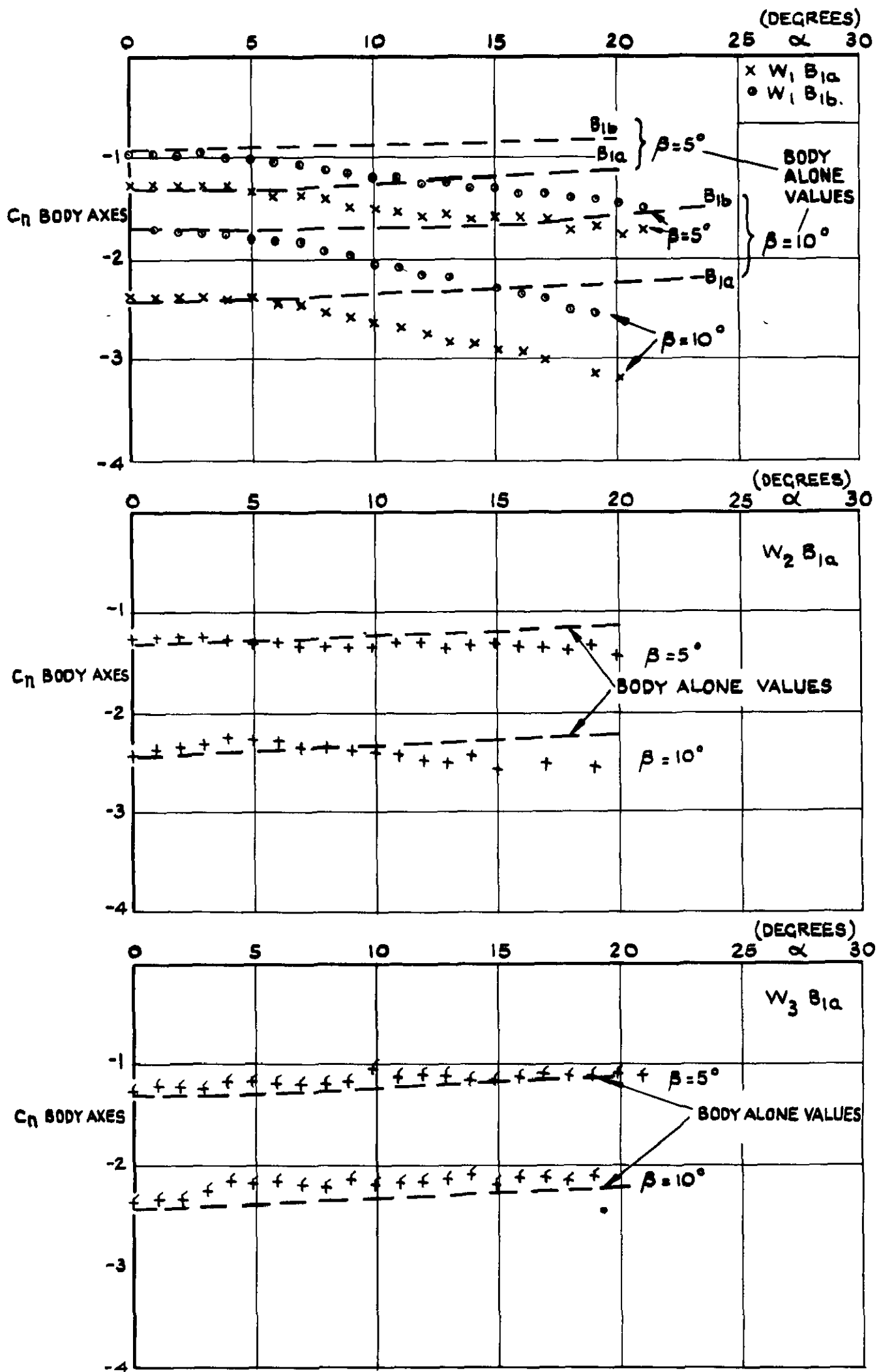


FIG. 14. YAWING MOMENT COEFFICIENT REFERRED TO BODY AXES.

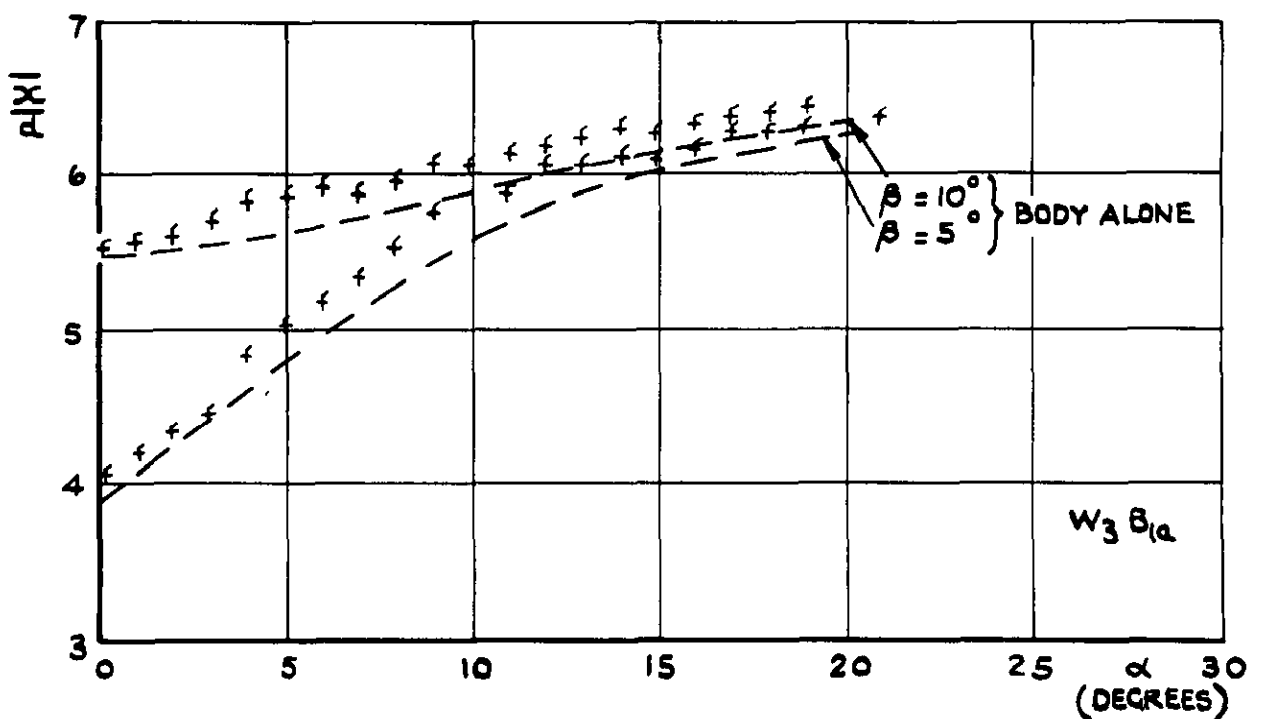
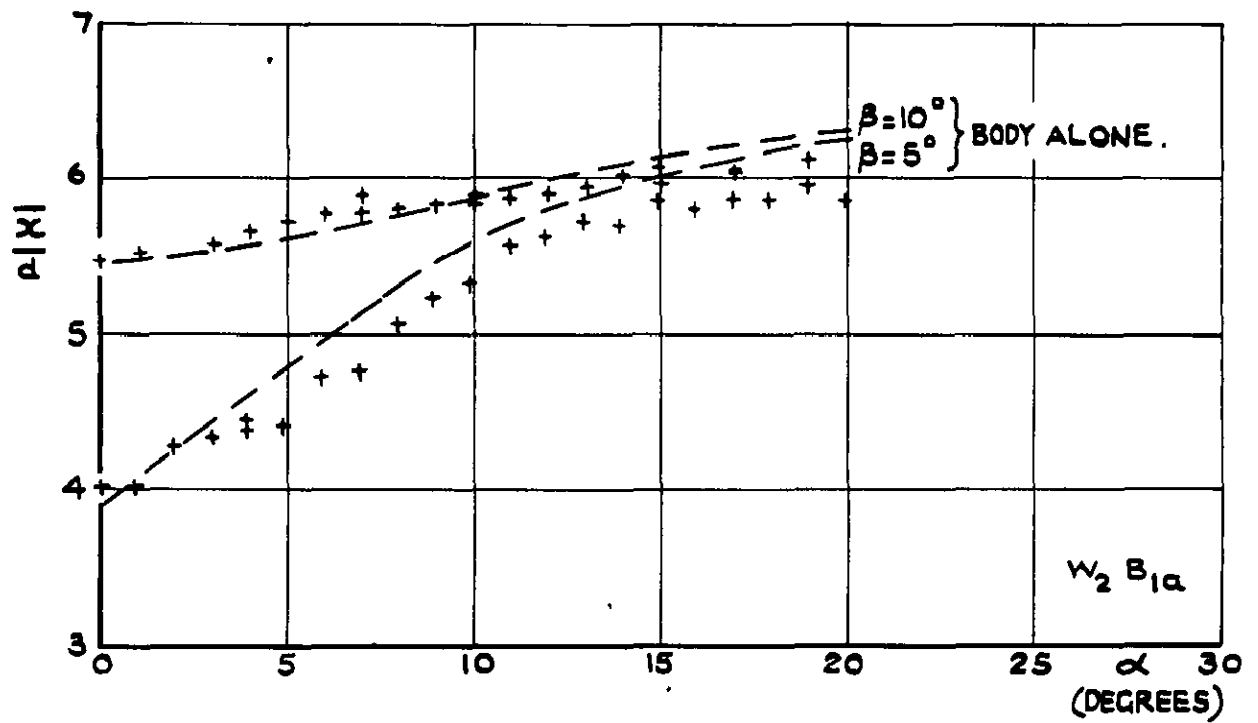
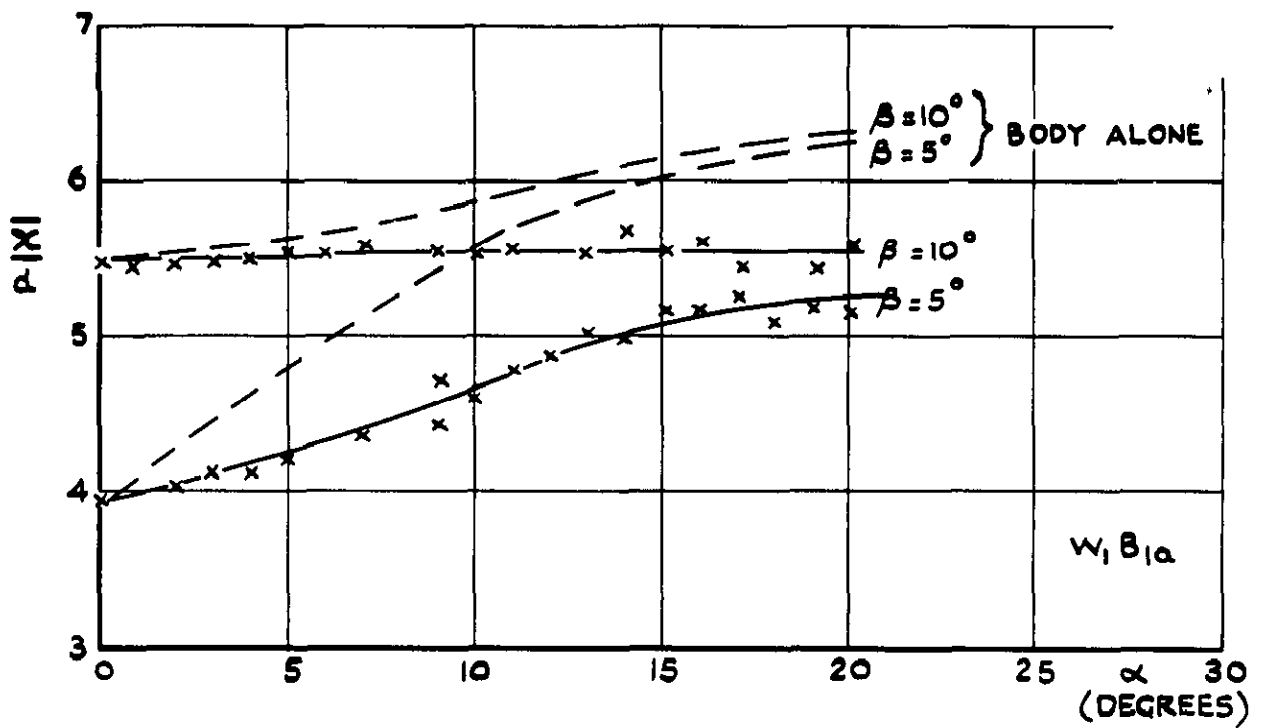


FIG.15. CENTRE OF PRESSURE OF SIDE FORCE.

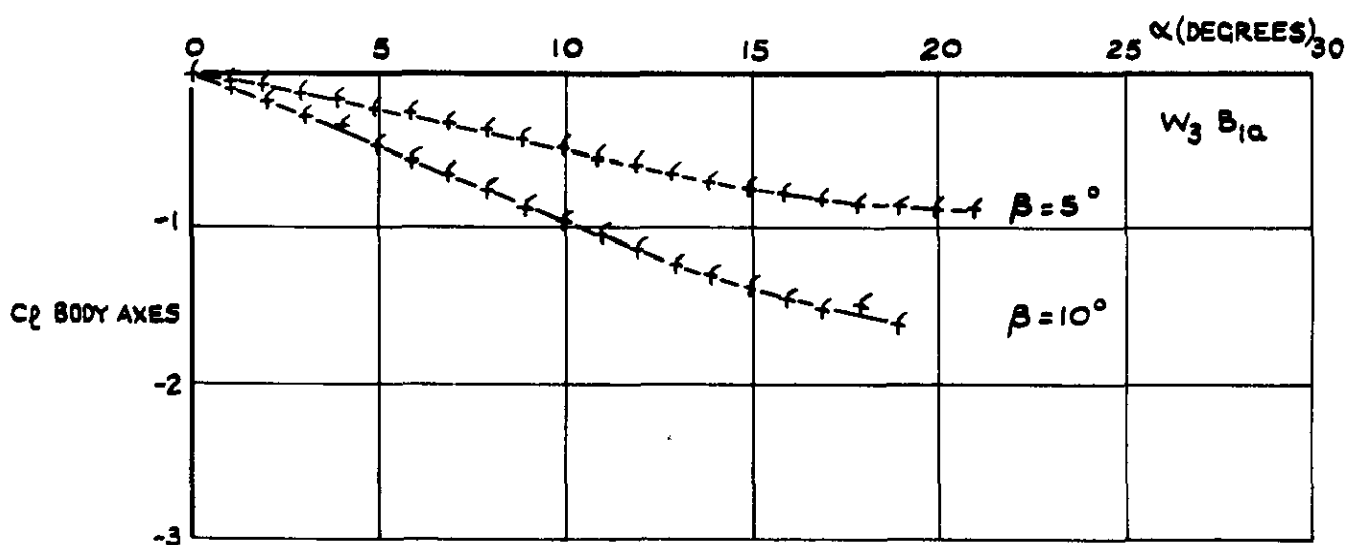
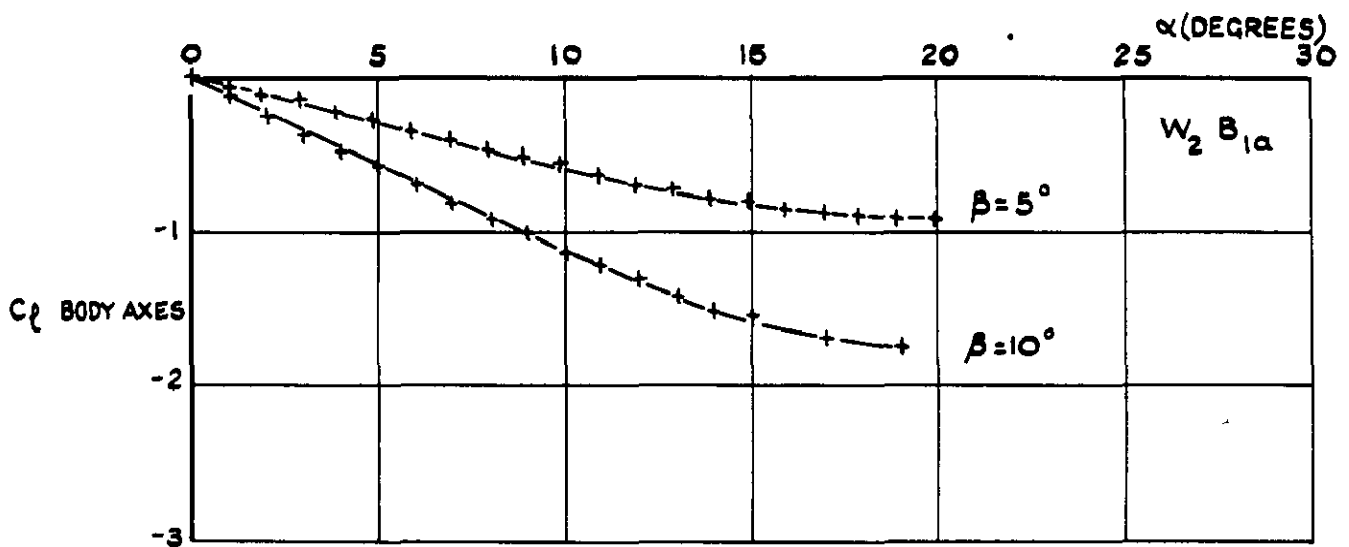
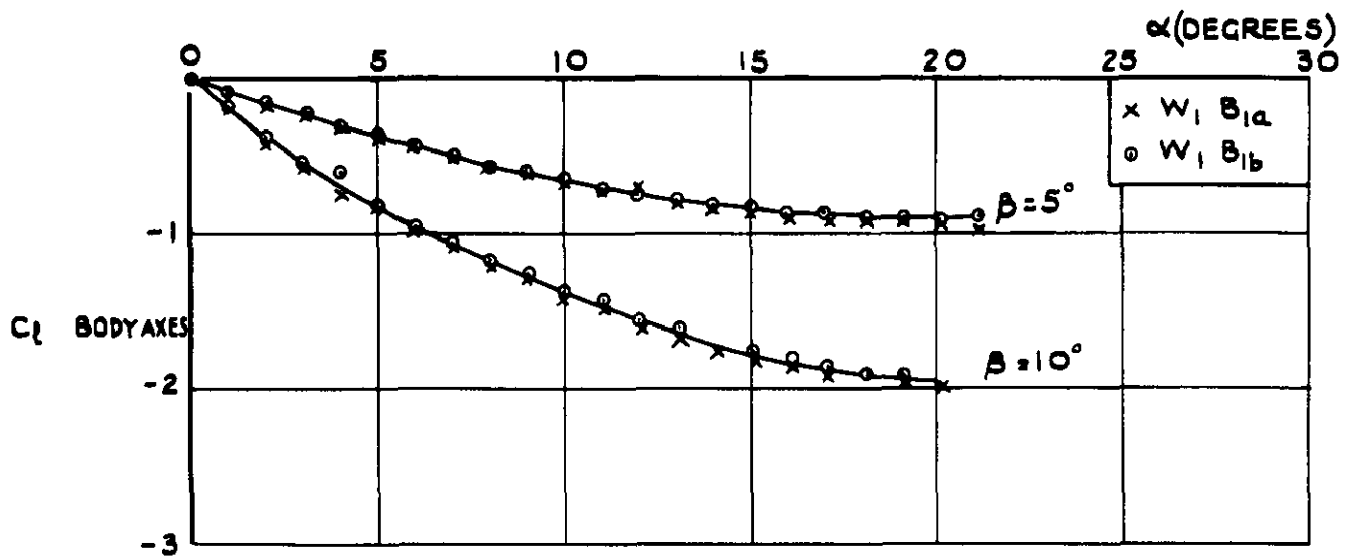
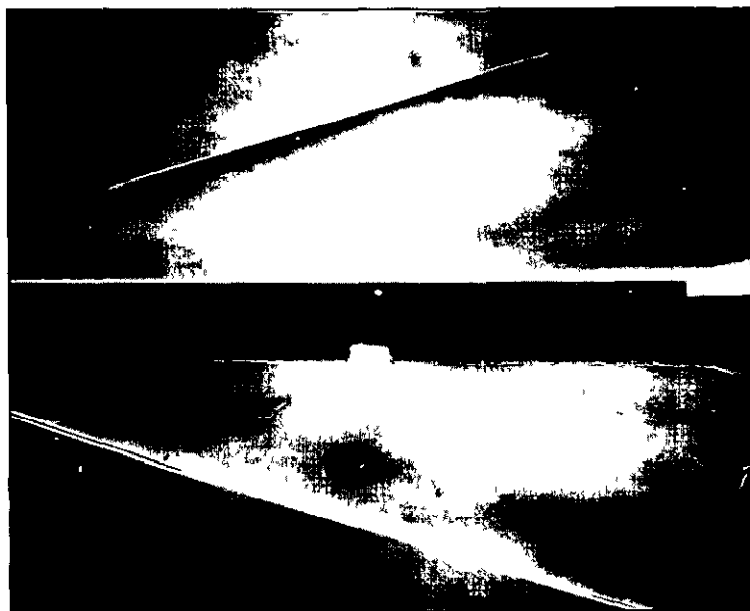
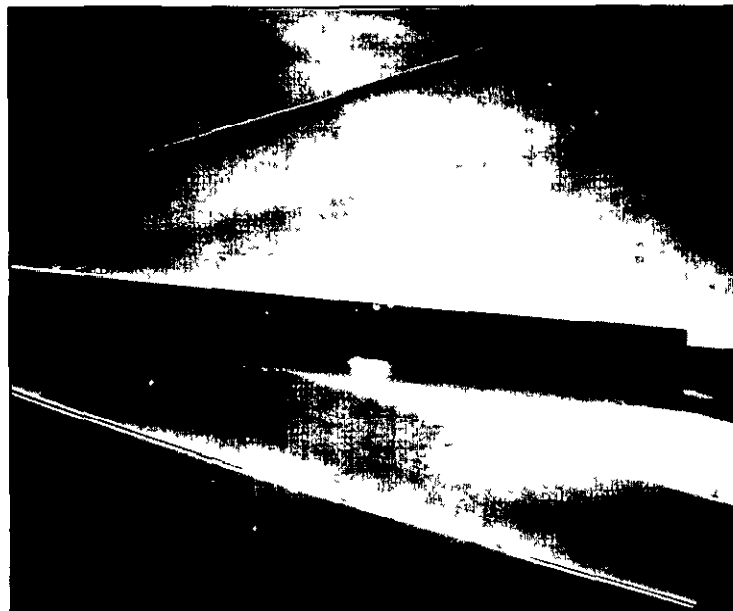


FIG. 16. ROLLING MOMENT COEFFICIENT REFERRED TO BODY AXES.



$\alpha = 0$



BODY SHOCK

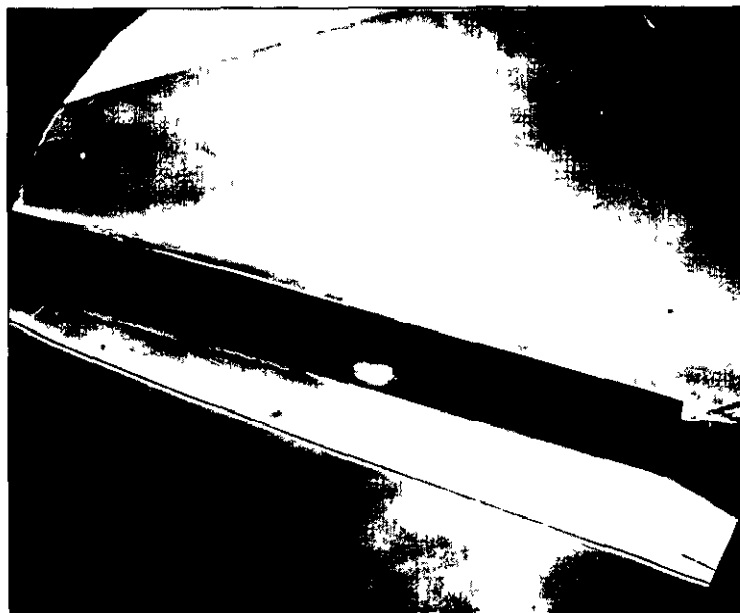
$\alpha = 6^\circ$

BODY VORTICES

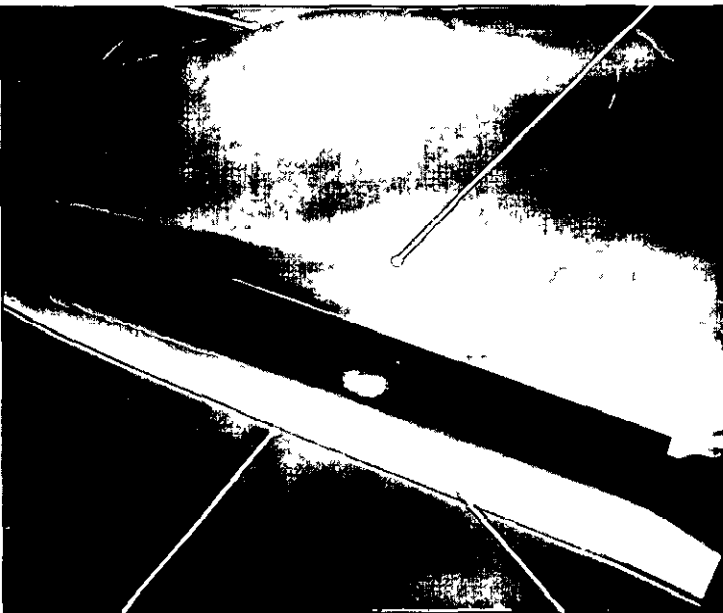


$\alpha = 10^\circ$

FLOW FROM LEFT TO RIGHT



$\alpha = 16^\circ$



BODY SHOCK

$\alpha = 20^\circ$

WING SHOCK

FIG 17. SCHLIEREN PHOTOS SHOWING SIDE VIEW OF MODEL WITH 3 CALIBRE NOSE AND ASPECT RATIO 1.03 WING ($B_{1\alpha}W_2$) AT ZERO SIDESLIP

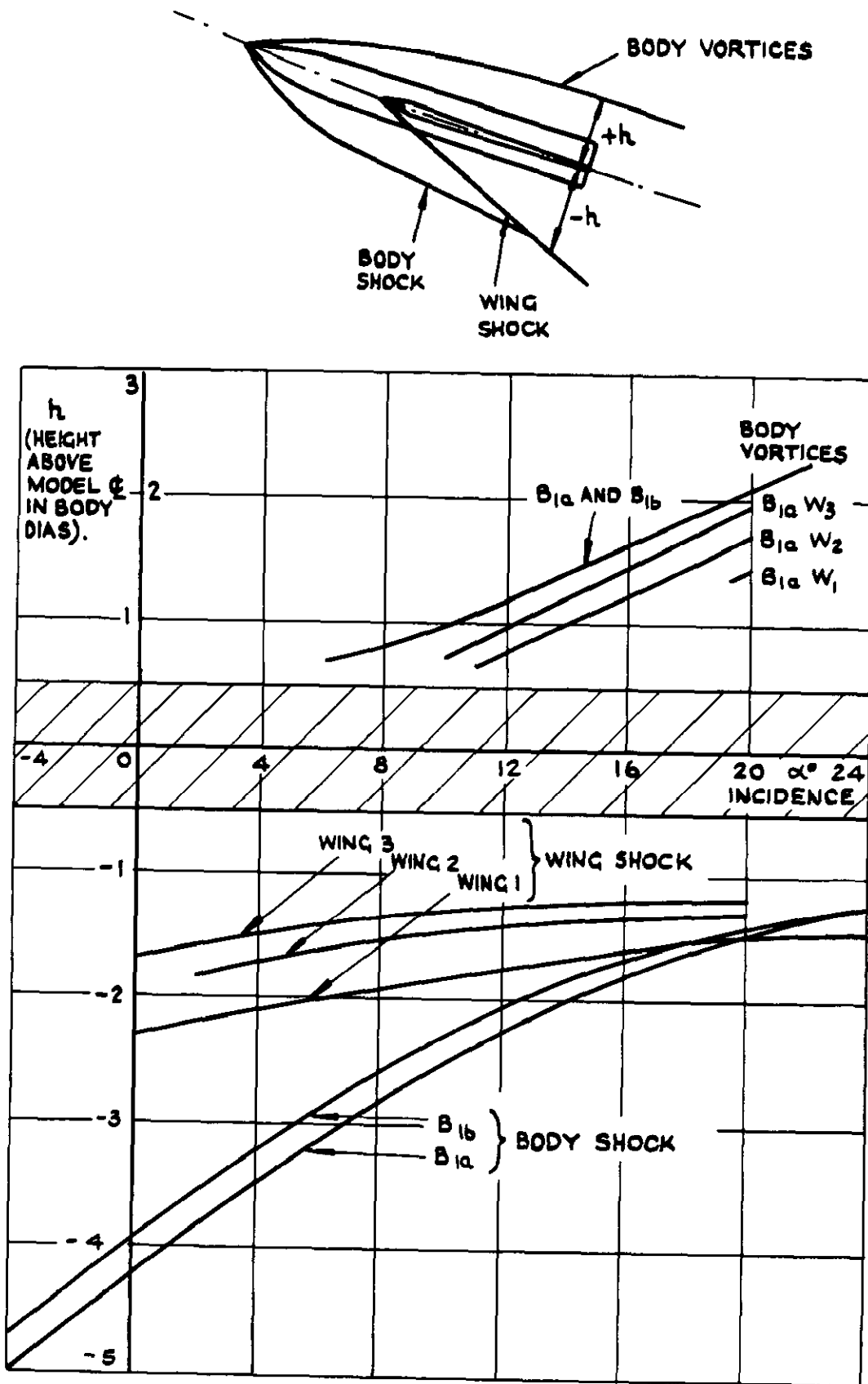


FIG. 18. LOCATION OF BODY VORTICES AND WING AND BODY SHOCKS.
(a) AT BODY BASE.

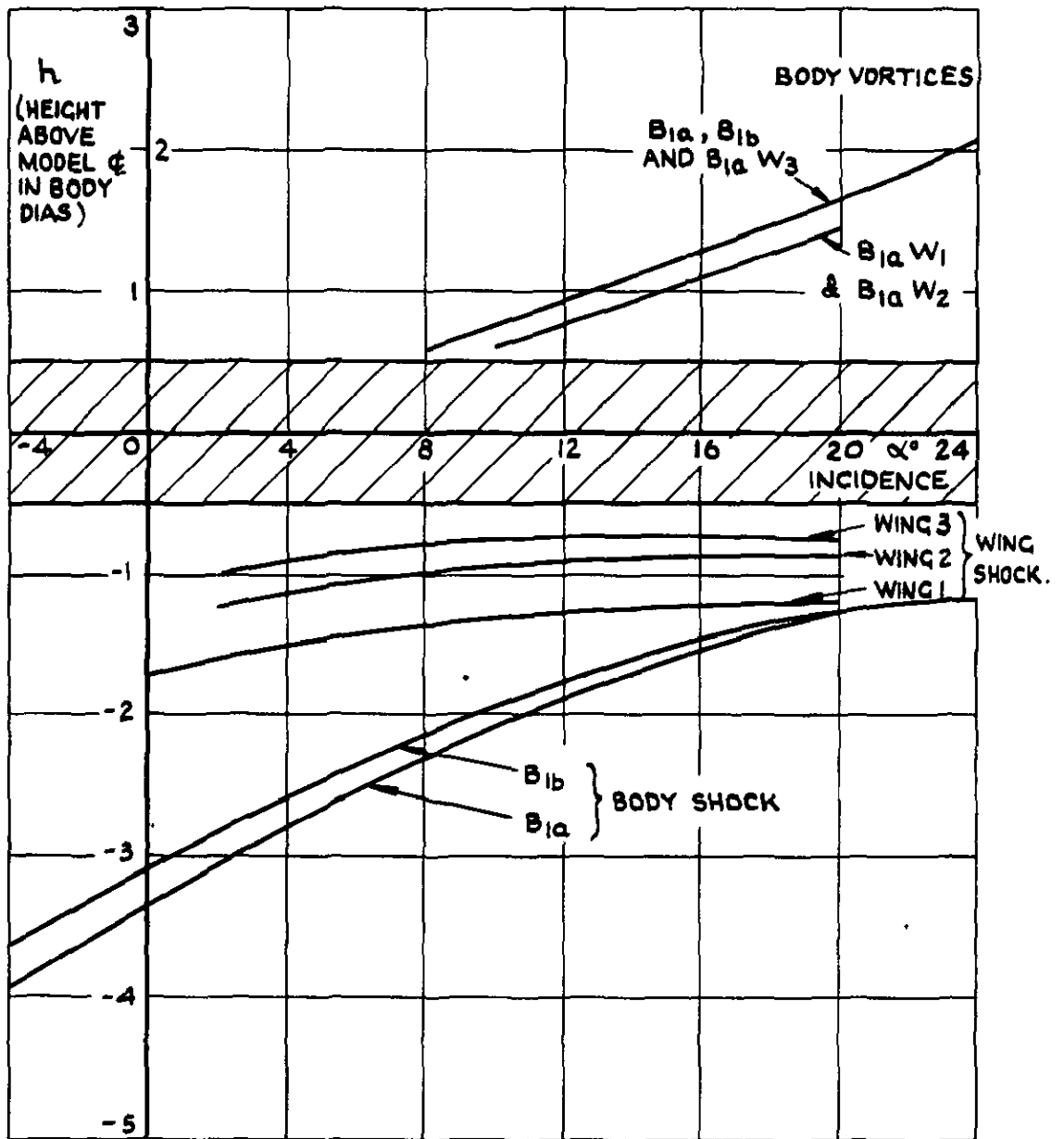


FIG. 18. (CONTD.)

(b) AT 3 BODY DIAS. UPSTREAM OF BODY BASE.

A.R.C. C.P. No. 888

AERODYNAMIC STUDY - FORCE AND MOMENT MEASUREMENTS ON
THREE DELTA WINGS OF ASPECT RATIOS 0.83, 1.03 and 1.24
IN COMBINATION WITH BODIES OF FINENESS RATIO 13 AT
A MACH NUMBER OF 4
Andrews, D.R., April 1962

Force measurements have been made in the High Supersonic Speed
Wind tunnel on a series of wing-body configurations at a Mach number
of 4 and Reynolds number of 32×10^6 . The combinations tested consisted

P.T.O.

533.695.12 :
533.693.3 :
533.6.013.1 :
533.6.011.5

A.R.C. C.P. No. 888

AERODYNAMIC STUDY - FORCE AND MOMENT MEASUREMENTS ON
THREE DELTA WINGS OF ASPECT RATIOS 0.83, 1.03 and 1.24
IN COMBINATION WITH BODIES OF FINENESS RATIO 13 AT
A MACH NUMBER OF 4
Andrews, D.R., April 1962

Force measurements have been made in the High Supersonic Speed
Wind tunnel on a series of wing-body configurations at a Mach number
of 4 and Reynolds number of 32×10^6 . The combinations tested consisted

P.T.O.

533.695.12 :
533.693.3 :
533.6.013.1 :
533.6.011.5

A.R.C. C.P. No. 888

AERODYNAMIC STUDY - FORCE AND MOMENT MEASUREMENTS ON
THREE DELTA WINGS OF ASPECT RATIOS 0.83, 1.03 and 1.24
IN COMBINATION WITH BODIES OF FINENESS RATIO 13 AT
A MACH NUMBER OF 4
Andrews, D.R., April 1962

Force measurements have been made in the High Supersonic Speed
Wind tunnel on a series of wing-body configurations at a Mach number
of 4 and Reynolds number of 32×10^6 . The combinations tested consisted

P.T.O.

DETACHABLE ABSTRACT CARDS

of circular section bodies of fineness ratio 13 and delta wings of aspect ratios 0.83, 1.03 and 1.24. The wing span of all combinations was 5 body diameters.

Lift and pitching moment variations with incidence were found to be reasonably linear up to 20° , which was the limit of the present tests. The highest lift drag ratio was obtained with the lowest aspect ratio wing, giving a figure of 5.7 for a 3 calibre ogival nose on the body and 6.2 for a 5 calibre nose. It was found that the force and moment characteristics could in general be predicted adequately from existing theories, the main exception being the rolling moment due to sideslip.

of circular section bodies of fineness ratio 13 and delta wings of aspect ratios 0.83, 1.03 and 1.24. The wing span of all combinations was 5 body diameters.

Lift and pitching moment variations with incidence were found to be reasonably linear up to 20° , which was the limit of the present tests. The highest lift drag ratio was obtained with the lowest aspect ratio wing, giving a figure of 5.7 for a 3 calibre ogival nose on the body and 6.2 for a 5 calibre nose. It was found that the force and moment characteristics could in general be predicted adequately from existing theories, the main exception being the rolling moment due to sideslip.

of circular section bodies of fineness ratio 13 and delta wings of aspect ratios 0.83, 1.03 and 1.24. The wing span of all combinations was 5 body diameters.

Lift and pitching moment variations with incidence were found to be reasonably linear up to 20° , which was the limit of the present tests. The highest lift drag ratio was obtained with the lowest aspect ratio wing, giving a figure of 5.7 for a 3 calibre ogival nose on the body and 6.2 for a 5 calibre nose. It was found that the force and moment characteristics could in general be predicted adequately from existing theories, the main exception being the rolling moment due to sideslip.

© Crown Copyright 1966

Published by
HER MAJESTY'S STATIONERY OFFICE

To be purchased from
49 High Holborn, London w c 1
423 Oxford Street, London w 1
13A Castle Street, Edinburgh 2
109 St Mary Street, Cardiff
Brazennose Street, Manchester 2
50 Fairfax Street, Bristol 1
35 Smallbrook, Ringway, Birmingham 5
80 Chichester Street, Belfast 1
or through any bookseller